Supporting Information to

Electronic Control of Spin-Crossover Properties in Four-Coordinate Bis(formazanate) Iron(II) Complexes

Francesca Milocco, Folkert de Vries, Imke M. A. Bartels, Remco W. A. Havenith, Jordi Cirera, Serhiy Demeshko, Franc Meyer and Edwin Otten

Contents

General Considerations

All manipulations were carried out under nitrogen or argon using standard glovebox, Schlenk, and vacuum-line techniques. THF (Aldrich, anhydrous, 99.8%) was dried by percolation over columns of Al_2O_3 (Fluka); toluene, hexane and pentane (Aldrich, anhydrous, 99.8%) were passed over columns of Al_2O_3 (Fluka), BASF R3-11-supported Cu oxygen scavenger, and molecular sieves (Aldrich, 4 Å). THF-d_8 (Euriso-top) and C_6D_6 (Aldrich) were vacuum transferred from Na/K alloy and stored under nitrogen.
The compounds PhNNC(*p*-Tol)NNHPh,[1] Fe[N(SiMe$_3$)$_2$]$_2$[2] were synthesized according to literature procedures. PhNNCPhNNHPh (TCI, 92 %) was washed with cold methanol and dried under vacuum before use. 4-fluorophenylhydrazine hydrochloride (TCI, 97 %), triethylamine (Sigma-Aldrich, 99 %), *p*-tolualdehyde(Sigma-Aldrich, 97 %), sodium carbonate (Merck), tetrabutylammonium bromide (Sigma-Aldrich, 99 %), 4-fluoroaniline (TCI, 98 %), hydrochloric acid (Boom B.V., 37–38 %), sodium nitrite (Sigma-Aldrich, 99 %) were used as received.
NMR spectra were recorded on a Varian Mercury 400, Inova 500, or Bruker 600 spectrometer. The ^{1}H and ^{13}C NMR spectra were referenced internally using the residual solvent resonances and reported in ppm relative to TMS (0 ppm). The assignments of NMR resonances were aided by COSY, HMQC, HSQC and HMBC experiments using standard pulse sequences.
Elemental analyses for organic compounds were performed at the Microanalytical Department of the University of Groningen, and the iron complexes were measured by the analytical laboratory of the Institute of Inorganic Chemistry at the University of Göttingen using an Elementar Vario EL III instrument.

Synthesis of the ligands

(C$_6$H$_4$(*p*-F))NNC(*p*-Tol)H.[3] 4-fluorophenylhydrazine hydrochloride (2.44 g, 15 mmol) was suspended in ethanol (50 mL). Addition of triethylamine (1.52 g, 15 mmol) led to a caramel-colored solution, to which *p*-tolualdehyde (1.80 g) was added. After stirring the suspension for 2h 30 min, 100 mL of water was added to the reaction mixture resulting in an immediate precipitation of a yellow solid. The suspension was stirred for 1 h and then the yellow solid was filtered and washed with water and cold hexane, to obtain 3.12 g of product (13.7 mmol, yield 91 %). It should be noted that the product is somewhat sensitive to hydrolysis: NMR analysis of solutions in 'wet' NMR solvents indicated the presence of multiple products, while analysis in anhydrous C_6D_6 showed a single product with resonances in agreement with the proposed hydrazone.
^{1}H-NMR (400 MHz, C_6D_6, 25 °C): δ 7.56 (d, J=8.2 Hz, 2H, *p*-Tol *o*-CH), 7.06 (d, J=7.9 Hz, 2H, *p*-Tol *m*-CH), 6.93-6.87 (m, 2H, C$_6$H$_4$(*p*-F) *m*-CH), 6.85-6.80 (m, 3H, C$_6$H$_4$(*p*-F) *o*-CH + N=CH), 6.49 (s, 1H, NH), 2.12 (s, 3H, *p*-Tol CH$_3$) ppm. ^{19}F-NMR (376 MHz, C_6D_6, 25 °C): δ -124.97 (m) ppm. ^{13}C-NMR (151 MHz, C_6D_6, 25 °C): δ 157.7 (d, $^1J_{C\text{-}F}$=237.1 Hz, C$_6$H$_4$(*p*-F) *ipso* C-F), 141.7 (d, $^4J_{C\text{-}F}$ =2.0 Hz C$_6$H$_4$(*p*-F) *ipso* C-NH), 138.5 (*p*-Tol *ipso* C-CH$_3$), 137.7 (N=C-H), 133.4 (*p*-Tol *ipso* C-C=N), 129.7 (*p*-Tol *m*-CH), 126.5 (*p*-Tol *o*-CH), 116.0 (d, $^2J_{C\text{-}F}$ =22.5 Hz, C$_6$H$_4$(*p*-F) *m*-CH), 114.0 (d, $^3J_{C\text{-}F}$ =7.3 Hz, C$_6$H$_4$(*p*-F) *o*-CH), 21.34 (*p*-Tol CH$_3$) ppm.
Anal. Calcd. for $C_{24}H_{13}FN_2$: C, 73.66; H, 5.74; N, 12.27. Found: C, 73.36; H 5.76; N, 12.12.

(C$_6$H$_4$(*p*-F))NNC(*p*-Tol)NNH(C$_6$H$_4$(*p*-F)) (2H). The hydrazone (C$_6$H$_5$F)NNC(*p*-Tol)H (3.10 g, 13.6 mmol) was suspended in a roundbottom flask with water (100 mL). Dichloromethane (100 mL), sodium carbonate (4.41 g, 43.5 mmol) and tetrabutylammonium bromide (0.44 g, 1.4 mmol) were added and the reaction mixture was stirred at 0 °C for 10 minutes.
In a separate flask, 4-fluoroaniline (1.51 g, 13.6 mmol), water (20 mL) and hydrochloric acid (3.4 mL) were mixed at 0 °C. A solution of sodium nitrite (1.0 g, 15.0 mmol) in water (10 mL) at 0 °C was added dropwise

to give a clear solution. After stirring for 30 min at 0 °C the solution with the *in situ* prepared diazonium salt was added dropwise to the first flask containing the hydrazone solution which subsequently turned from yellow to blood red.
After stirring for 2 h at r.t. the organic layer was separated and the water layer was extracted with CH_2Cl_2 (2 x 150 mL) and the combined organic phase was washed with water (3 x 150 mL).
The cherry red colored solution was concentrated under reduced pressure. The product was purified by recrystallization (CH_2Cl_2/MeOH) and 1.14 g of dark purple solid was obtained (3.2 mmol, yield 24%).
^{1}H-NMR (600 MHz, C_6D_6, 25 °C): δ 15.09 (s, 1H, NH) 8.26 (d, J=8.0 Hz, 2H, *p*-Tol *o*-CH), 7.29-7.26 (m, 6H, *p*-Tol *m*-CH + C_6H_4(*p*-F) *o*-CH), 6.85-6.81 (m, 4H, C_6H_4(*p*-F) *m*-CH), 2. 42 (s, 3H, *p*-Tol CH_3) ppm. ^{19}F-NMR (376 MHz, C_6D_6, 25 °C): δ -113.94 (m, C_6H_4(*p*-F)) ppm. ^{13}C-NMR (151 MHz, C_6D_6, 25 °C): δ 162.2 (d, $^1J_{C\text{-}F}$=247.6 Hz, C_6H_4(*p*-F) *ipso* C-F), 144.6 (d, $^4J_{C\text{-}F}$ =2.8 Hz C_6H_4(*p*-F) *ipso* C-NH), 141.9 (*ipso* N-C=N), 137.9 (*p*-Tol *ipso* C-CH_3), 135.2 (*p*-Tol *ipso* C-C=N), 129.6 (*p*-Tol *m*-CH), 126.5 (*p*-Tol *o*-CH), 120.6 (d, $^3J_{C\text{-}F}$ =8.2 Hz, C_6H_4(*p*-F) *o*-CH), 116.4 (d, $^2J_{C\text{-}F}$ =23.0 Hz, F-C_6H_4 *m*-CH), 21.3 (*p*-Tol CH_3) ppm.
Anal. Calcd. for $C_{20}H_{16}F_2N_4$: C, 68.56; H, 4.60; N, 15.99. Found: C, 68.24; H 4.64; N, 15.63.

(*p*-An)NNC(Ph)NNH(*p*-An) (3H). Compound **3H** was prepared according to the literature procedure.[4] For completeness, its NMR spectral data are listed below.
^{1}H-NMR (600 MHz, C_6D_6, 25 °C): δ 15.67 (s, 1H, NH) 8.44 (m, 2H, Ph *o*-CH), 7.56 (m, 4H, *p*-An *o*-CH), 7.42 (m, 2H, Ph *m*-CH), 7.26 (tt, ^{1}J=7.3 Hz, ^{2}J=1.2 Hz, 1H, Ph *p*-CH), 6.81 (m, 4H, *p*-An *m*-CH), 3.30 (m, 6H, *p*-An OCH_3) ppm. ^{13}C-NMR (151 MHz, C_6D_6, 25 °C): δ 159.7 (*p*-An *ipso* C-OCH_3), 142.4 *p*-An *ipso* C-N), 141.3 (*ipso* N-C=N), 138.7 (Ph *ipso* C), 128.7 (Ph *m*-CH), 127.7 (Ph *p*-CH), 126.4 (Ph *o*-CH), 120.6 (*p*-An *o*-CH), 115.0 (*p*-An *m*-CH), 55.1 (*p*-An OCH_3) ppm.

PhNNC(C_6H_4(*p*-F))NNHPh (4H). Compound **4H** was prepared according to the literature procedure.[5] For completeness, its NMR spectral data are listed below.
^{1}H-NMR (600 MHz, $CDCl_3$, 25 °C): 15.39 (br, 1H, NH), 8.11 (m, 2H, C_6H_4(*p*-F) *o*-CH), 7.68 (d, J=7.8 Hz, 4H, Ph *o*-CH), 7.46 (t, J=7.8 Hz, 4H Ph *m*-CH), 7.29 (t, J = 7.3 Hz, 2H, Ph *p*-CH), 7.13 (t, J = 8.6 Hz, 2H, C_6H_4(*p*-F) *m*-CH) ppm. ^{19}F-NMR (376 MHz, C_6D_6, 25 °C): δ -115.05 (m, C_6H_4(*p*-F)) ppm. ^{13}C-NMR (151 MHz, C_6D_6, 25 °C): δ 162.9 (d, $^1J_{C\text{-}F}$=246.7 Hz, C_6H_4(*p*-F) *ipso* C-F), 148.0 (Ph, *ipso*) 140.7 (*ipso* N-C=N), 133.7 (C_6H_4(*p*-F) *ipso* C), 129.6 (Ph, *m*-CH), 127.7 (Ph, *p*-CH + C_6H_4(*p*-F) *o*-CH), 118.9 (Ph, *o*-CH), 115.4 (d, $^2J_{C\text{-}F}$ =21.9 Hz, F-C_6H_4 *m*-CH) ppm.

PhNNC(*p*-An)NNHPh (5H). Compound **5H** was prepared according to the literature procedure.[6] For completeness, its NMR spectral data are listed below.
^{1}H-NMR (200 MHz, $CDCl_3$, 25 °C): δ 15.23 (s, 1H, NH) 8.07 (d, 2H, J = 8.5 Hz, *p*-An *o*-CH), 7.68 (d, 4H, J = 7.9 Hz, Ph *o*-CH), 7.45 (t, 4H, J = 7.7 Hz, Ph *m*-CH), 7.28 (d, 2H, J = 8.5 Hz, Ph *p*-CH), 6.99 (m, 2H, *p*-An *m*-CH), 3.87 (s, 3H, *p*-An OCH_3) ppm. ^{13}C-NMR (50 MHz, $CDCl_3$, 25 °C): δ 159.47 *p*-An *ipso* C-OCH_3), 147.98 *p*-An *ipso*-C), 141.21 (*ipso* N-C=N), 130.21 (Ph *ipso*-C), 129.39 (Ph *m*-CH), 127.28 (Ph *m*-CH + *p*-An *o*-CH), 118.70 (Ph *o*-CH) , 113.81 *p*-An *m*-CH), 55.37 *p*-An OCH_3) ppm.

Compound **1** was reported previously *via* salt metathesis.[7] A more convenient method was developed by protonolysis of $Fe[N(SiMe_3)_2]_2$, and is reported below for **1**.

$Fe[PhNNC(p\text{-}Tol)NNPh]_2$ (1). A THF (40 mL) solution of **L1H** (1.84 g, 5.86 mmol) was added to a green solution of $Fe[N(SiMe_3)_2]_2$ (1.10 g, 2.93 mmol) in 20 mL of THF. The reaction mixture was stirred for 3 days at room temperature leading to a burgundy solution. The volatiles were removed under *vacuum* and the obtained crude product was dissolved in hot hexane (100 mL) and was slowly cooled down to −30 °C overnight affording compound **1** as dark red powder (1.68 g, 2.46 mmol, 84% yield). The identity of the product was confirmed by ^{1}H-NMR spectroscopy, which showed a spectrum that was identical to the compound prepared via salt metathesis.

Single crystal X-ray data

Table S1. Selected bond lengths (Å) and angles (°) in compounds 1-6 at 100 K.

	1[a]	2	3	4	5	6
Fe(1)–N(1)	1.8278(15)	1.816(2)	1.819(4)	1.8154(19)	1.8470(11)	1.9532(15)
Fe(1)–N(4)	1.8207(15)	1.819(2)	1.830(4)	1.8159(19)	1.8360(11)	1.9780(15)
Fe(1)–N(5)	1.8330(16)	1.826(2)		1.8211(19)	1.8183(11)	1.9812(15)
Fe(1)–N(8)	1.8174(16)	1.809(2)		1.8205(19)	1.8246(11)	1.9801(15)
N(1)-N(2)	1.327(2)	1.331(3)	1.321(6)	1.316(2)	1.3313(14)	1.314(2)
N(3)-N(4)	1.329(2)	1.330(3)	1.328(6)	1.321(2)	1.3270(15)	1.311(2)
N(5)-N(6)	1.328(2)	1.322(3)		1.327(2)	1.3294(14)	1.315(2)
N(7)-N(8)	1.327(2)	1.331(3)		1.325(2)	1.3306(15)	1.304(2)
∠(NFeN)/(NFeN)[b]	60.97(10)	58.81(15)	59.4(3)	62.35(12)	69.38(7)	89.15(9)
Fe out-of-plane[c]	0.001 0.046	0.037 0.040	0.033	0.005 0.009	0.010 0.052	0.068 0.414

[a] Data taken from ref [7]. [b] Dihedral angle between the coordination planes defined by the N-Fe-N atoms. [c] Displacement of the Fe atom out of the plane defined by the 4 N atoms of each ligand backbone.

Table S2. Crystallographic data for compounds 2-6.

	2	3	4	5	6
chem formula	$C_{40}H_{30}F_4FeN_8$	$C_{42}H_{38}FeN_8O_4$	$C_{38}H_{28}F_2FeN_8$	$C_{40}H_{34}Fe\ N_8O_2$	$C_{38}H_{30}FeN_8$
M_r	754.57	774.65	690.53	714.61	654.55
cryst syst	triclinic	monoclinic	triclinic	monoclinic	monoclinic
color, habit	dark red, plate	dark red, needle	dark red, block	dark red, block	dark red, plate
size (mm)	0.24 x 0.17 x 0.07	0.23 x 0.09 x 0.05	0.20 x 0.16 x 0.15	0.26 x 0.23 x 0.13	0.14 x 0.12 x 0.02
space group	P -1	C 2/c	P -1	P 21/n	P 21/c
a (Å)	10.7043(4)	18.8670(8)	8.783(3)	13.0505(4)	15.1516(5)
b (Å)	13.6484(6)	9.9736(4)	11.110(4)	16.0146(5)	12.1817(4)
c (Å)	14.3016(6)	21.0794(8)	17.438(5)	17.4162(5)	16.9830(6)
α (°)	81.388(3)	90	87.54(2)	90	90
β (°)	78.691(2)	112.918(2)	83.79(2)	101.7610(10)	92.7330(10)
γ (°)	81.445(2)	90	71.55(2)	90	90
V (Å³)	2010.33(15)	3653.4(3)	1604.6(9)	3563.54(19)	3131.03(18)
Z	2	4	2	4	4
ρ_{calc}, g.cm^{-3}	1.247	1.408	1.429	1.269	1.389
Radiation [Å]	Cu K_α 1.54178	Cu K_α 1.54178	Mo K_α 0.71073	Mo K_α 0.71073	Cu K_α 1.54178
μ(Mo K_α), mm^{-1}			0.524	0.468	
μ(Cu K_α), mm^{-1}	3.481	3.766			4.193

F(000)	776	1616	712	1353	1360
Temp (K)	100(2)	100(2)	100(2)	100(2)	100(2)
θ range (°)	3.18 – 65.34	4.56 – 65.20	3.03 – 27.10	3.00 – 28.71	2.92 – 70.17
data collected (h,k,l)	-12:12; -16:16; -16:16	-22:20; 0:11; 0:24	-11:11; -14:14; 0:22	-17:17; -21:21; -23:23	-18:18; -14:13; -20:20
no. of rflns collected	25255	3060	13912	113018	25816
no. of indpndt collected	6777	3060	13912	9224	5886
Observed reflns $F_o \geq 2.0\ \sigma(F_o)$	5820	2786	12051	7643	5463
R(F) (%)	4.97	6.33	3.94	3.26	3.43
wR(F^2) (%)	11.32	17.29	10.70	8.40	8.49
GooF	1.051	1.133	1.086	1.022	1.044
weighting a,b	0.0215, 3.4680	0.0837, 16.6108	0.0395, 1.1355	0.0353, 2.2701	0.0331, 2.4692
params refined	480	252	443	537	424
min, max resid dens	-0.506, 0.366	-0.390, 1.148	-0.517, 0.585	-0.366, 0.454	-0.426, 0.315

Table S3. VT-Xray data of compound 5: selected bond lengths (Å) and angles (°).

	100	**150**	**200**	**250**	**293**	**325**	**350**	**375**	**400**	**425**	**293[b]**
Fe(1)–N(1)	1.8480 (15)	1.8479 (16)	1.8482 (15)	1.8502 (16)	1.8546 (18)	1.865 (2)	1.880 (2)	1.902 (3)	1.921 (3)	1.944 (7)	1.830 (3)
Fe(1)–N(4)	1.8329 (15)	1.8339 (16)	1.8339 (15)	1.8352 (16)	1.8415 (18)	1.853 (2)	1.869 (2)	1.889 (3)	1.910 (3)	1.923 (7)	1.836 (3)
Fe(1)–N(5)	1.8151 (15)	1.8173 (15)	1.8171 (15)	1.8184 (16)	1.8242 (17)	1.836 (2)	1.854 (2)	1.876 (2)	1.896 (3)	1.917 (7)	1.817 (3)
Fe(1)–N(8)	1.8240 (15)	1.8238 (15)	1.8236 (15)	1.8265 (16)	1.8308 (17)	1.840 (2)	1.855 (2)	1.877 (3)	1.894 (3)	1.941 (6)	1.836 (3)
N(1)-N(2)	1.329 (2)	1.329 (2)	1.328 (2)	1.328 (2)	1.325 (2)	1.323 (3)	1.322 (3)	1.317 (3)	1.316 (4)	1.310 (8)	1.328 (3)
N(3)-N(4)	1.325 (2)	1.326 (2)	1.326 (2)	1.326 (2)	1.325 (2)	1.321 (3)	1.319 (3)	1.319 (3)	1.314 (4)	1.311 (8)	1.326 (3)
N(5)-N(6)	1.326 (2)	1.326 (2)	1.3253 (19)	1.325 (2)	1.323 (2)	1.320 (3)	1.319 (3)	1.320 (3)	1.317 (4)	1.310 (8)	1.326 (3)
N(7)-N(8)	1.330 (2)	1.329 (2)	1.331 (2)	1.328 (2)	1.328 (2)	1.326 (3)	1.326 (3)	1.324 (3)	1.319 (4)	1.308 (8)	1.337 (4)
∠(NFeN) /(NFeN)[a]	69.37 (7)	69.49 (10)	69.57 (9)	69.96 (10)	70.58 (11)	71.72 (13)	73.19 (14)	75.02 (15)	76.57 (18)	77.75 (40)	70.27 (17)

[a] Dihedral angle between the coordination planes defined by the N-Fe-N atoms. [b] Measured after heating to 450K, which causes loss of the disordered solvent molecule

Table S4. Crystallographic data for the VT X-ray study of 5.[a]

	100	150	200	250	293	325	350	375	400	425	293
chem formula	$C_{40}H_{34}Fe\,N_8O_2$										
M_r	714.60										
cryst syst	monoclinic										
color, habit	dark red, block										
size (mm)	0.62 x 0.36 x 0.08										
space group	P 21/n										
Radiation [Å]	Mo K_α 0.71073										
a (Å)	13.0356 (4)	13.0621 (4)	13.097 (6)	13.137 (5)	13.1666 (7)	13.204 (16)	13.252 (4)	13.324 (6)	13.365 (8)	13.305 (12)	12.7743 (12)
b (Å)	16.0219 (6)	16.0581 (6)	16.094 (9)	16.110 (8)	16.1319 (9)	16.119 (2)	16.104 (5)	16.119 (8)	16.116 (11)	16.197 (16)	15.9993 (15)
c (Å)	17.4226 (6)	17.4579 (6)	17.505 (9)	17.555 (8)	17.6152 (10)	17.705 (2)	17.843 (5)	17.998 (9)	18.101 (11)	18.326 (16)	17.8511 (17)
α (°)	90	90	90	90	90	90	90	90	90	90	90
β (°)	101.6510 (10)	101.4960 (10)	101.338 (2)	101.154 (2)	100.981 (2)	100.793 (5)	100.514 (12)	100.213 (19)	99.93 (3)	100.07 (4)	102.280 (3)
γ (°)	90	90	90	90	90	90	90	90	90	90	90
V (Å³)	3563.8 (2)	3588.4 (2)	3616.4 (3)	3644.6 (3)	3673.0 (4)	3700.7 (8)	3743.8 (19)	3804 (3)	3840 (4)	3888 (6)	3564.9 (6)
Z	4	4	4	4	4	4	4	4	4	4	4
ρ_{calc}, g.cm^{-3}	1.332	1.323	1.312	1.302	1.292	1.283	1.268	1.248	1.236	1.221	1.331
μ(Mo K_α), mm^{-1}	0.471	0.467	0.464	0.460	0.457	0.453	0.448	0.441	0.437	0.431	0.470
F(000)	1488	1488	1488	1488	1488	1488	1488	1488	1488	1488	1488
Temp (K)	100(2)	150(2)	200(2)	249(2)	293(2)	325(2)	350(2)	375(2)	400(2)	425(2)	292(2)
θ range (°)	3.00 – 27.16	2.99 – 27.13	2.99 – 27.07	2.98 – 27.08	2.98– 26.87	2.98 – 27.10	2.97 – 26.94	2.97 – 26.59	2.96 – 26.54	2.96 – 23.79	3.02 – 24.51
data collected (h,k,l)	-16:16; -20:20; -22:22	-16:16; -20:20; -22:22	-16:16; -20:20; -22:22	-16:16; -20:20; -22:22	-16:16; -20:20; -22:22	-16:16; -20:20; -22:22	-16:16; -20:20; -22:22	-16:16; -20:20; -22:22	-17:16; -20:20; -23:22	-15:15; -19:19; -21:21	-15:15; -18:18; -20:20
no. of rflns collected	48571	48935	48919	49678	49967	50077	50151	50615	50699	37825	37444
no. of indpndt collected	7892	7938	7983	8061	8112	8154	8197	8277	8445	6574	6048
Observed reflns $F_o \geq 2.0\,\sigma(F_o)$	6242	6166	6136	5959	5759	5398	5124	4846	4435	3252	3602
R(F) (%)	3.74	3.86	3.76	3.97	4.27	4.69	5.00	5.42	6.10	12.63	4.98
wR(F^2) (%)	9.33	9.77	9.73	10.40	11.80	10.65	14.40	15.82	19.11	32.42	11.60
GooF	1.062	1.059	1.042	1.041	1.045	1.035	1.062	1.063	1.047	1.815	1.041
weighting a,b	0.0269, 4.6236	0.0298, 4.1066	0.0333, 3.2322	0.0357, 3.0495	0.0453, 2.6836	0.0497, 3.1263	0.0529, 2.8746	0.0570, 2.8142	0.0666, 3.7919	0.1000	0.0352, 2.8668
params refined	537	537	537	537	537	537	537	537	494	494	462
min, max resid dens	-0.404, 0.438	-0.361, 0.427	-0.379, 0.273	-0.364, 0.269	-0.369, 0.229	-0.350, 0.256	-0.317, 0.272	-0.312, 0.267	-0.304, 0.308	-0.597, 1.151	-0.279, 0.292

[a] All structures measure at 100 – 425K contain a disordered THF solvent molecule, the contribution of which was removed using PLATON/SQUEEZE: it is not included in the molecular formula. The data in the last column (293K) are after heating to 450K, upon which the solvent molecule is lost.

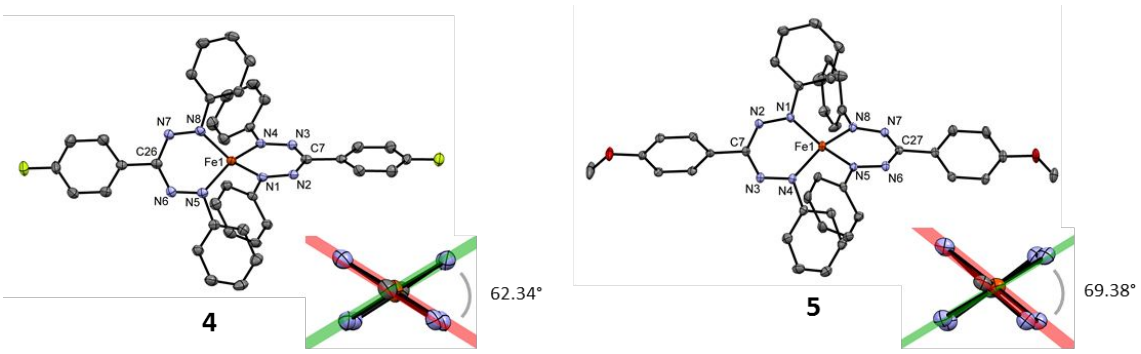

Figure S1. Molecular structure of compounds **4** and **5** showing 50% probability ellipsoids. Hydrogen atoms are omitted for clarity. The inset for each shows the $Fe(NNCNN)_2$ core of the structure with the N-Fe-N planes and their dihedral angle.

X-ray powder diffraction

Powder X-ray diffraction data were collected using a Bruker D8 Advance diffractometer equipped with CuK_{α} source (λ = 1.5406 Å). The samples were placed on a powder specimen holder and sealed with a polyimide (Kapton) film inside the glovebox and subsequently taken out for analysis. The X-ray powder pattern were calculated from the crystal structure using *VESTA*.[8]

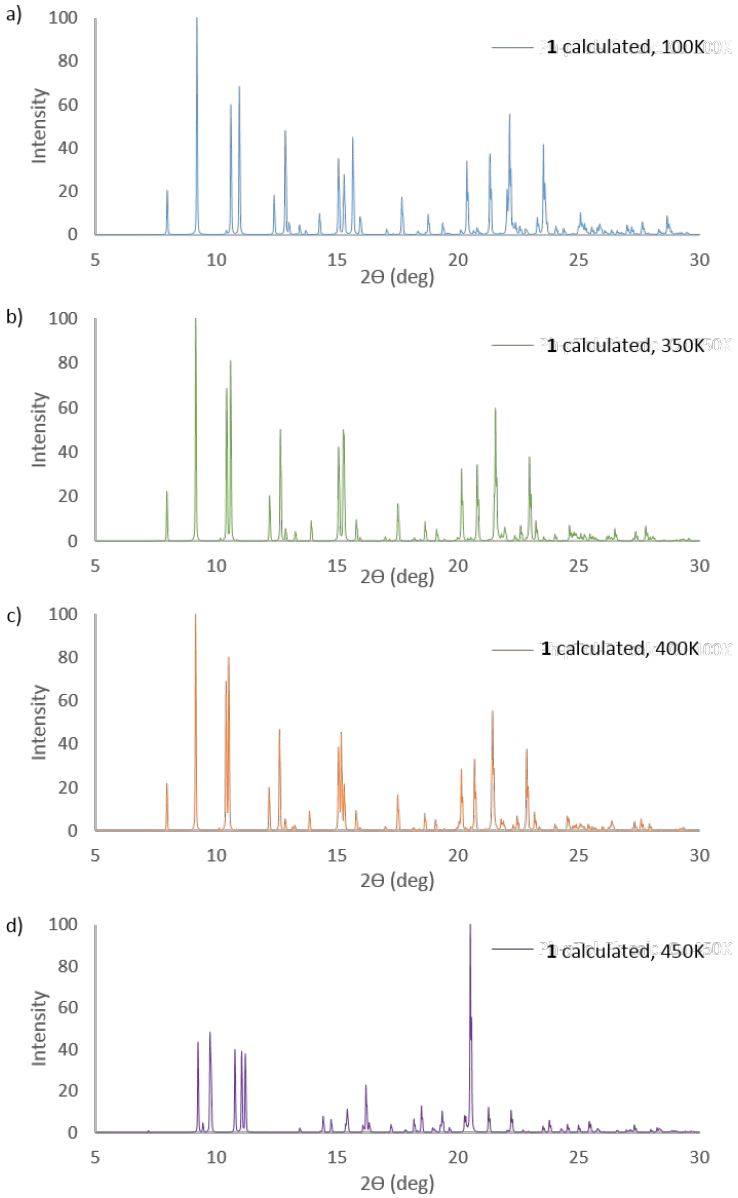

Figure S2. Calculated powder X-ray diffraction patterns of compound **1**[7] from crystal structure: a) 100K, b) 350K, c) 400K, d) 450K.

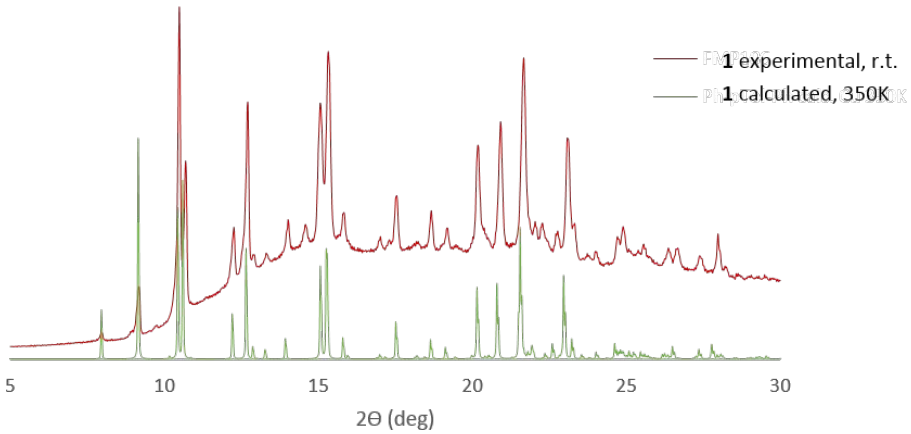

Figure S3. Powder X-ray diffraction patterns of compound **1**: experimental at room temperature, (red line) and calculated from crystal structure at 350K (green line).

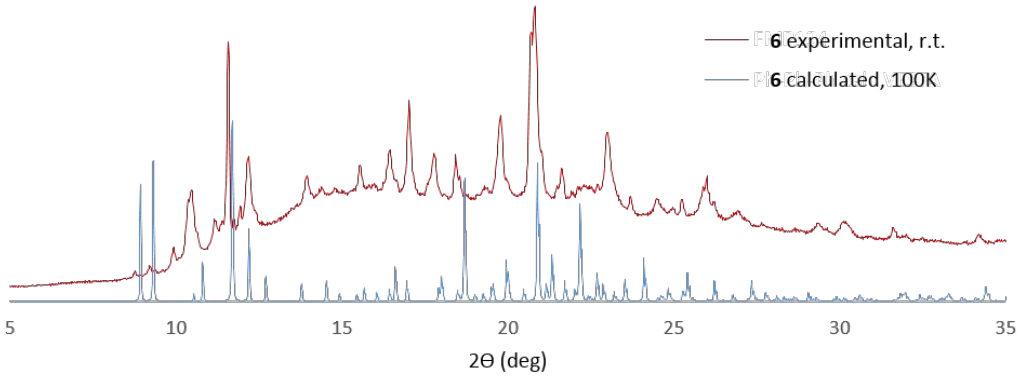

Figure S4. Powder X-ray diffraction patterns of compound **6**: experimental at room temperature, (red line) and calculated from crystal structure at 100K (blue line).

Mössbauer spectroscopy

Mössbauer spectra were recorded with a ^{57}Co source in a Rh matrix using an alternating constant acceleration *Wissel* Mössbauer spectrometer operated in the transmission mode and equipped with a *Janis* closed-cycle helium cryostat. Isomer shifts are given relative to iron metal at ambient temperature. Simulation of the experimental data was performed with the *Mfit* program: E. Bill, Max-Planck Institute for Chemical Energy Conversion, Mülheim/Ruhr, Germany.

The samples used for Mössbauer analysis were previously dried under vacuum.
It should be noted that some batch-to-batch variation was observed in the Mössbauer spectra (varying amounts of an additional doublet with isomer shift around 0.45-0.55 mm/s). To investigate whether decomposition of the compounds (by air/moisture) is responsible for this, we analysed a relatively clean batch of compound **5** by collecting Mössbauer data (80 K) on a sample handled in the glovebox (Figure S5a). In addition, from the same batch of **5**, an amount was exposed to air for 65 h and also measured at 80 K (Figure S5b). From a comparison of this data we conclude that the species with isomer shift at ca. 0.50 mm/s is due to decomposition under aerobic conditions.

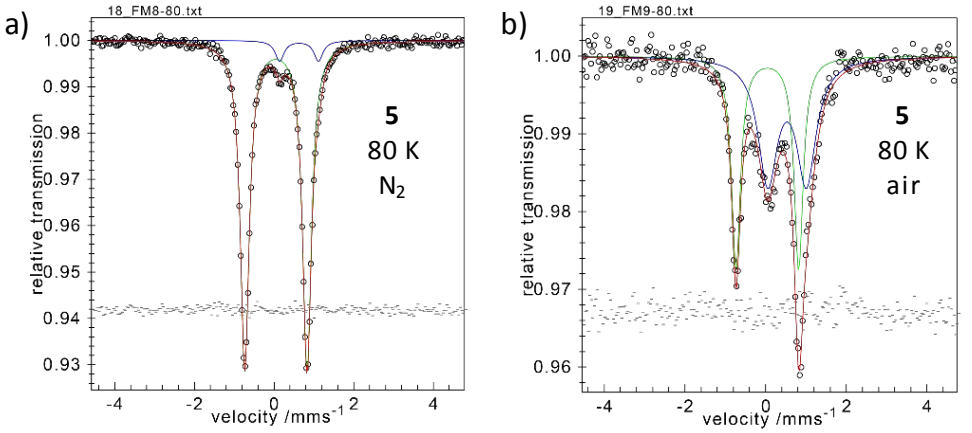

94.07 %
δ = 0.05 mm·s^{-1}, $|\Delta E_Q|$ = 1.56 mm·s^{-1}
5.93 %
δ = 0.63 mm·s^{-1}, $|\Delta E_Q|$ = 0.98 mm·s^{-1}

45.00 %
δ = 0.04 mm·s^{-1}, $|\Delta E_Q|$ = 1.55 mm·s^{-1}
55.00 %
δ = 0.53 mm·s^{-1}, $|\Delta E_Q|$ = 0.96 mm·s^{-1}

Figure S5. Comparison of Mössbauer spectra of **5** before (a) and after exposure to air for 65 h (b).

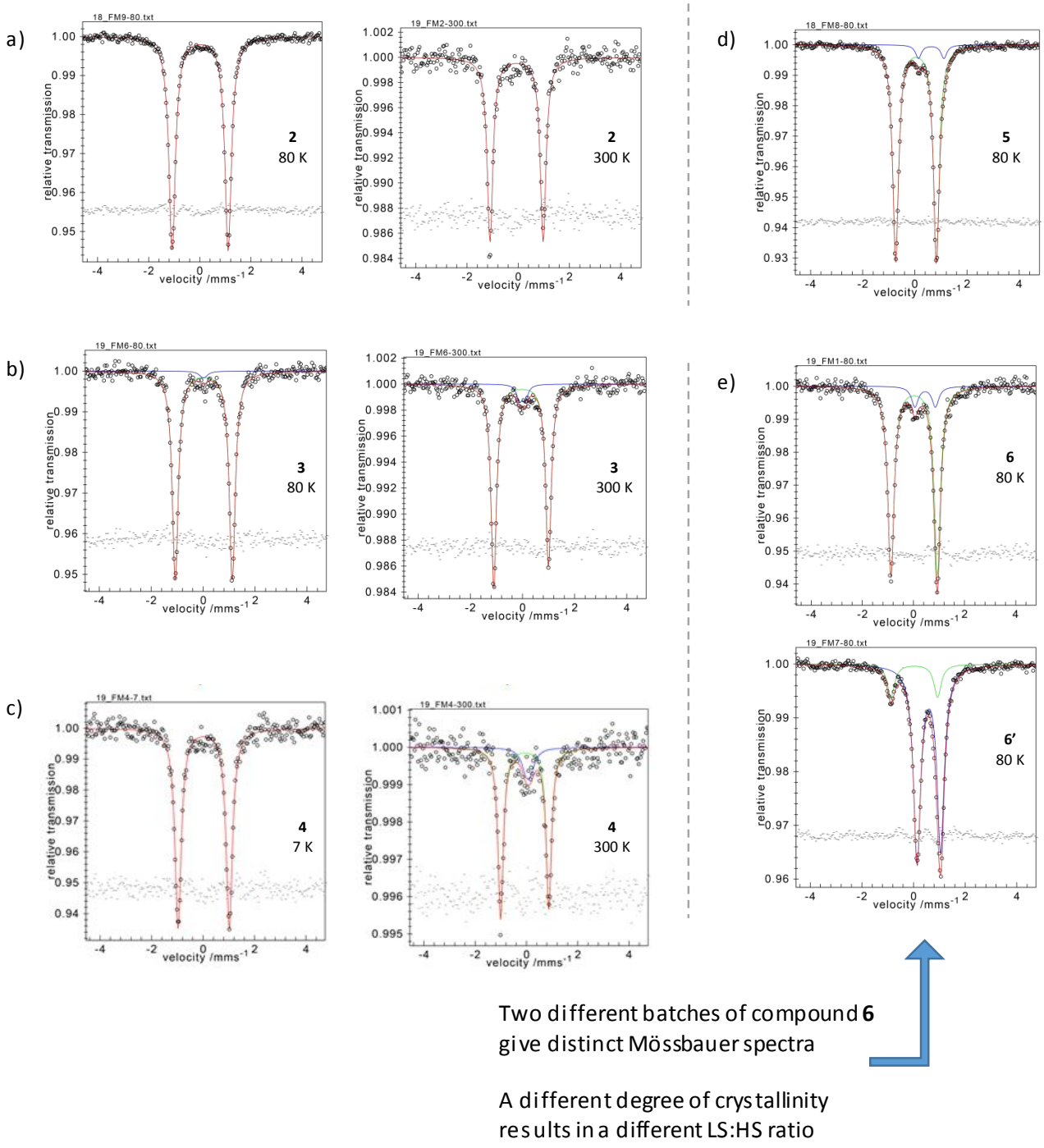

Figure S6. Mössbauer spectra of compounds **2**-**6** in the solid state.

Table S5. Mössbauer parameters (δ = isomer shift; ΔE_q = quadrupole splitting) for **2**-**6** in the solid state. Since the doublets of the minor species (less than 10 % rel. intensity) are not well resolved, the fit parameters of these species are somewhat arbitrary.

	T (K)	Rel %	δ (mm·s^{-1})	ΔEq (mm·s^{-1})
2	100	100	0.01	2.19
	300	100	- 0.07	2.07
3	80	98 2	0.02 0.01	2.19 0.10
	300	93 7	-0.05 -0.01	2.10 0.22
4	7	100	0.03	1.99
	300	84 16	- 0.07 0.07	1.86 0.17
5	80	94 6	0.05 0.63	1.56 0.98
6	7	100	0.03	1.82
	80	90 10	0.03 0.46	1.81 0.80
6' (different batch)	80	15 85	0.03 0.60	1.81 0.91

SQUID magnetometry

Temperature-dependent magnetic susceptibility measurements for **5** and **6'** in the solid state were carried out with a *Quantum-Design* MPMS-XL-5 SQUID magnetometer equipped with a 5 Tesla magnet in the range from 400 to 2.0 K at a magnetic field of 0.5 T. The powdered sample was contained in a Teflon bucket and fixed in a non-magnetic sample holder. Each raw data file for the measured magnetic moment was corrected for the diamagnetic contribution of the Teflon bucket according to $M^{dia}(\text{bucket}) = \chi_g \cdot m \cdot H$, with an experimentally obtained gram susceptibility of the Teflon bucket. The molar susceptibility data were corrected for the diamagnetic contribution. The samples used for SQUID measurement were previously dried under vacuum.

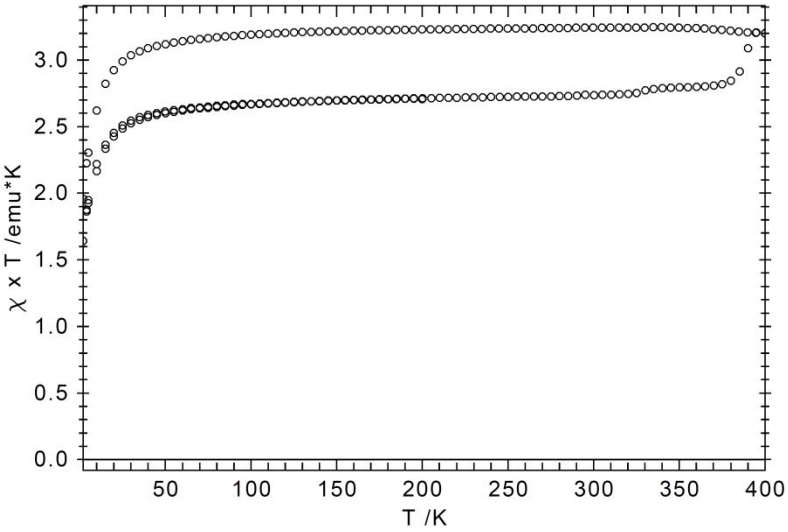

Figure S7. Magnetic susceptibility data for **6'** in the solid state with the temperature sequence 200 -> 2 -> 400 -> 2 K.

DSC

Differential scanning calorimetry (DSC) measurements were performed on a TA Instrument DSC Q100 equipped with a Refrigerated Cooling System (RSC) temperature controller. The samples were sealed in an aluminium Tzero pan with Tzero Hermetic Lid inside the glovebox and subsequently taken out for analysis. Heating/cooling rates were 10 °C/min.

The samples used for DSC measurement were previously dried under vacuum.

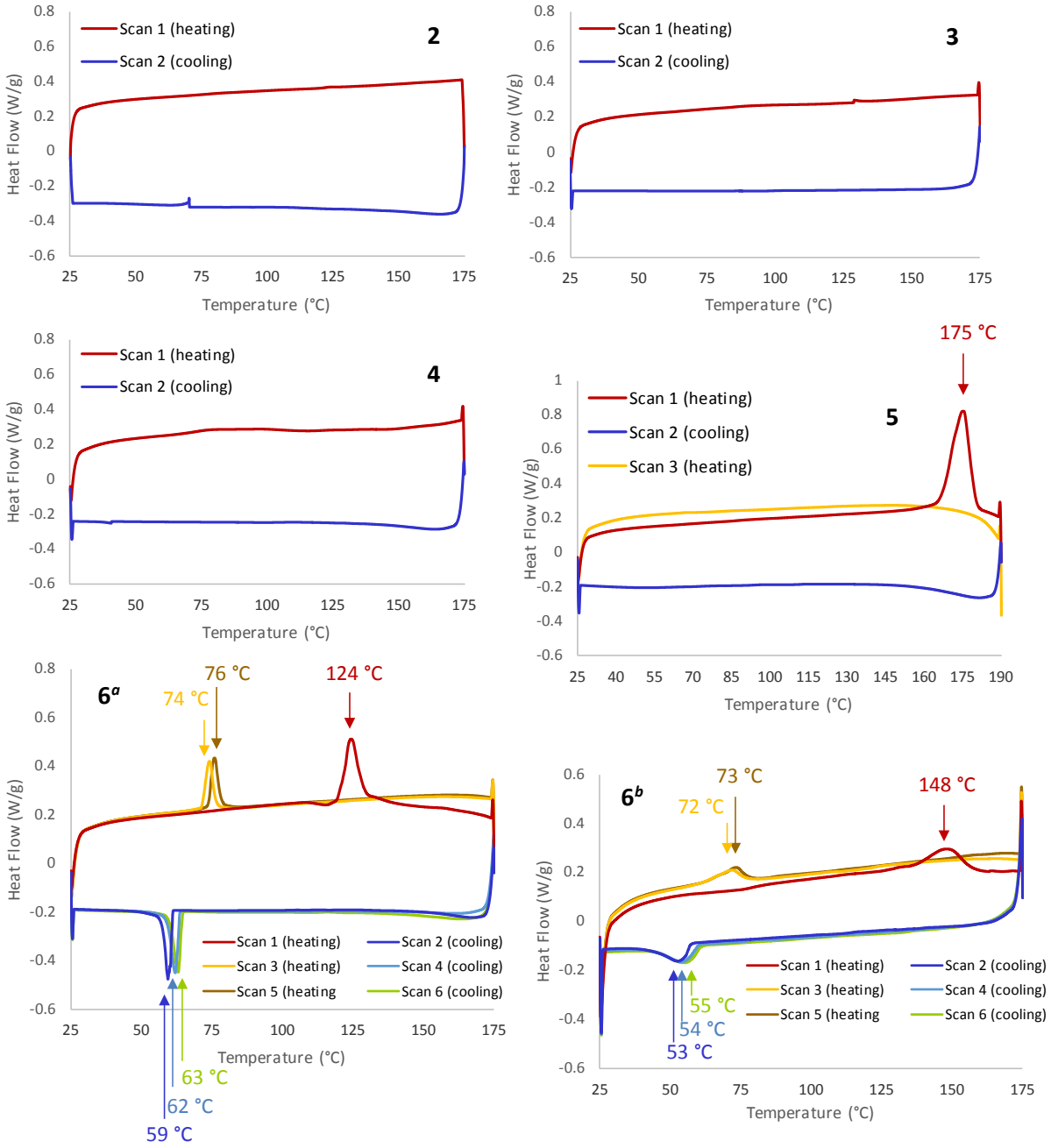

Figure S8. Differential scanning calorimetry measurements for **2-6**. For compounds **2, 3, 4**, **6**: heating cycle to 175 °C and cooling cycle to 25 °C and for compound **5**: heating cycle to 190 °C and cooling cycle to 25 °C. **6**^{a} is a crystalline sample and **6**^{b} is a powder sample obtained from grinding the crystals.

Analysis of the thermodynamic parameters for the spin crossover equilibrium

The thermodynamic parameters (ΔH and ΔS) that describe the spin state equilibrium in solution were determined by fitting the temperature-dependence of three independent sets of empirical data: (1) NMR chemical shifts (δ), (2) solution magnetic susceptibilities (χ) and (3) molar extinction coefficients (ε) from UV-Vis spectra.
Fitting was performed using Wolfram Mathematica 12,[9] as outlined below for each set of data. In general, these methods rely on eq S1, which describes the mole fraction of the high-spin state (γ_{HS}) as a function of temperature.[10]

(eq S1)
$$\gamma_{HS} = \frac{1}{\left(1 + e^{\frac{\Delta H}{RT} - \frac{\Delta S}{R}}\right)}$$

A comparison of the values obtained for ΔH and ΔS with the different methods is reported in Table S8 and a plot of the mole fraction of **2-6** in the HS state (γ_{HS}) vs. T is shown in Figure S27-28.

Analysis of temperature dependence of NMR chemical shifts

The temperature dependence of the chemical shift was measured via VT-NMR spectroscopy. The temperature at the sample position inside the spectrometer was calibrated using a temperature calibration sample with methanol (for low temperature) or ethylene glycol (for high temperature).[11] ^{1}H and ^{19}F NMR shifts were modelled according to the ideal solution model (equation S2).[10a,10b,12]

(eq S2)
$$\delta_{obs} = \delta_{LS} + \frac{C}{T\left(1 + e^{\frac{\Delta H}{RT} - \frac{\Delta S}{R}}\right)}$$

For each compound the data of all ^{1}H and ^{19}F (when applicable) resonances were fit using C, ΔH and ΔS as fitting parameters. The chemical shifts in the low-spin state (δ_{LS}) were constrained either to the value found in the diamagnetic zinc analogue (for **1**)[13] or to chemically reasonable values (for **2**-**6**).
For every compound, several (or all) of its NMR resonances were individually analysed to give multiple values for ΔH and ΔS. These values were subsequently averaged, and the standard deviation was taken from the set, to give the values reported in table 2 and table S8. $T_{½}$ was calculated (eq S3) and the uncertainty in $T_{½}$ was obtained using error propagation from ΔH and ΔS (eq S4).

(eq S3)
$$T_{\frac{1}{2}} = \frac{\Delta H}{\Delta S}$$

(eq S4)
$$\sigma_{T_{1/2}} = \left|T_{\frac{1}{2}}\right| \sqrt{\left[\frac{(\sigma_{\Delta H})^2}{(\Delta H)^2} + \frac{(\sigma_{\Delta S})^2}{(\Delta S)^2}\right]}$$

The empirical data points and fitted lines for each compound are shown below (Figure S9-21).

Analysis of temperature dependence of the magnetic susceptibility and of the molar extinction coefficient

The temperature dependence of the magnetic susceptibility (χ) was measured via the Evans method[14] by VT-NMR spectroscopy, and of the molar extinction coefficient (ε) by VT-UV-Vis spectroscopy.
The temperature dependence of the experimentally obtained x (with x = χ or ε) is attributed to the change of the mole fraction of molecules in the HS state γ_{HS} according to eq (S5)[7,10c] which can be rearranged as (S6):

(eq S5) $$x = x_{LS} + \gamma_{HS}(x_{HS} - x_{LS})$$

(eq S6) $$\gamma_{HS} = \frac{x - x_{LS}}{x_{HS} - x_{LS}}$$

Combining eq S6 with eq S1 give the analytical expression for the temperature dependence of x:

(eq S7) $$x = x_{LS} + \frac{1}{\left(1 + e^{\frac{\Delta H}{RT} - \frac{\Delta S}{R}}\right)}(x_{HS} - x_{LS})$$

Fitting of the data to eq S7 was performed using Mathematica. The errors for the thermodynamic parameters reported in Table S8 are the standard errors obtained from the non-linear fit of the temperature-dependent data (either χ or ε) to the model (eq S7). It should be noted that although the values for the standard error are in similar range as those found based on the NMR chemical shifts, the error estimate of the data based on χ or ε is obtained in a different way than that for the NMR data (see above).

The magnetic susceptibility measured for each compound by Evans method is reported in Table S6. The magnetic susceptibility for the low-spin state (χ_{LS}) and high spin state (χ_{HS}) were constrained to the spin only values.
The data points and fitted lines for the molar extinction coefficient are reported in Figure S24-26. The molar extinction coefficients for the low-spin state (ε_{LS}) and high spin state (ε_{HS}) are unknown because the transition is incomplete and therefore they have to be determined from a fit using (eq. S7), *e.g.* together with thermodynamic parameters Δ*H* and Δ*S*, four fitting parameters have to be adjusted (Table S8).
The magnetic susceptibility (χ) and the molar extinction coefficient (ε) were calculated taking into account the temperature dependent changes in effective concentration due to the change in density of the solvent with temperature.[15]

The temperature dependence of the density of THF was calculated using:
Dortmund Data Bank, 2017-2019, www.ddbst.com
http://ddbonline.ddbst.de/DIPPR105DensityCalculation/DIPPR105CalculationCGI.exe.
The temperature dependence of the density of THF-d_8 was calculated by scaling the above values according to the difference in density at r.t. between the deuterated and non-deuterated solvent.

NMR spectral data and analysis of temperature dependence of ^{1}H and ^{19}F NMR shifts

Note: Asterisks (*) in the NMR spectra indicate the residual resonances of THF-d_8 and a small amount of water in the sealed capillary, which as inserted in the NMR tube to obtain the temperature-dependence of the solution magnetic moment (Evans method).

VT-NMR analysis for Fe[PhNNC(p-Tol)NNPh]$_2$ (1)

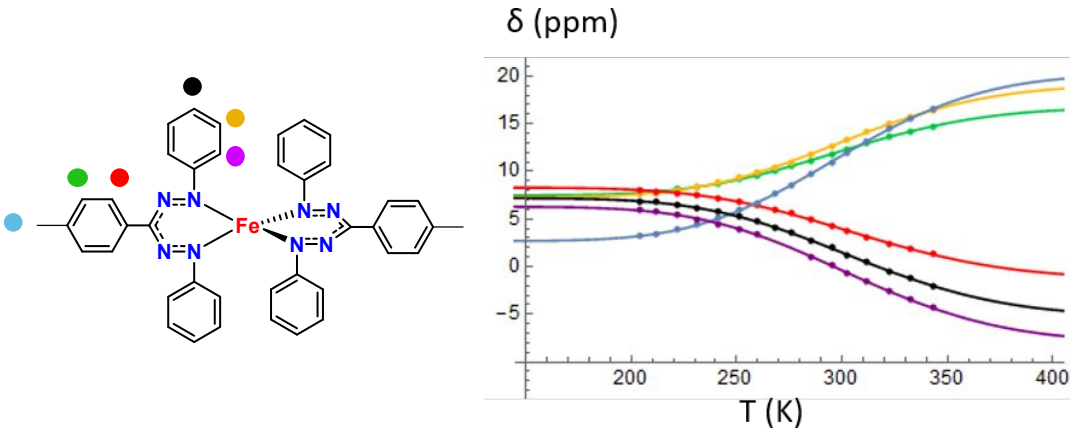

Figure S9. Temperature dependence of the ^{1}H NMR signals of **1** (THF-d_8 solution). Data fitted with the ideal solution model equation.

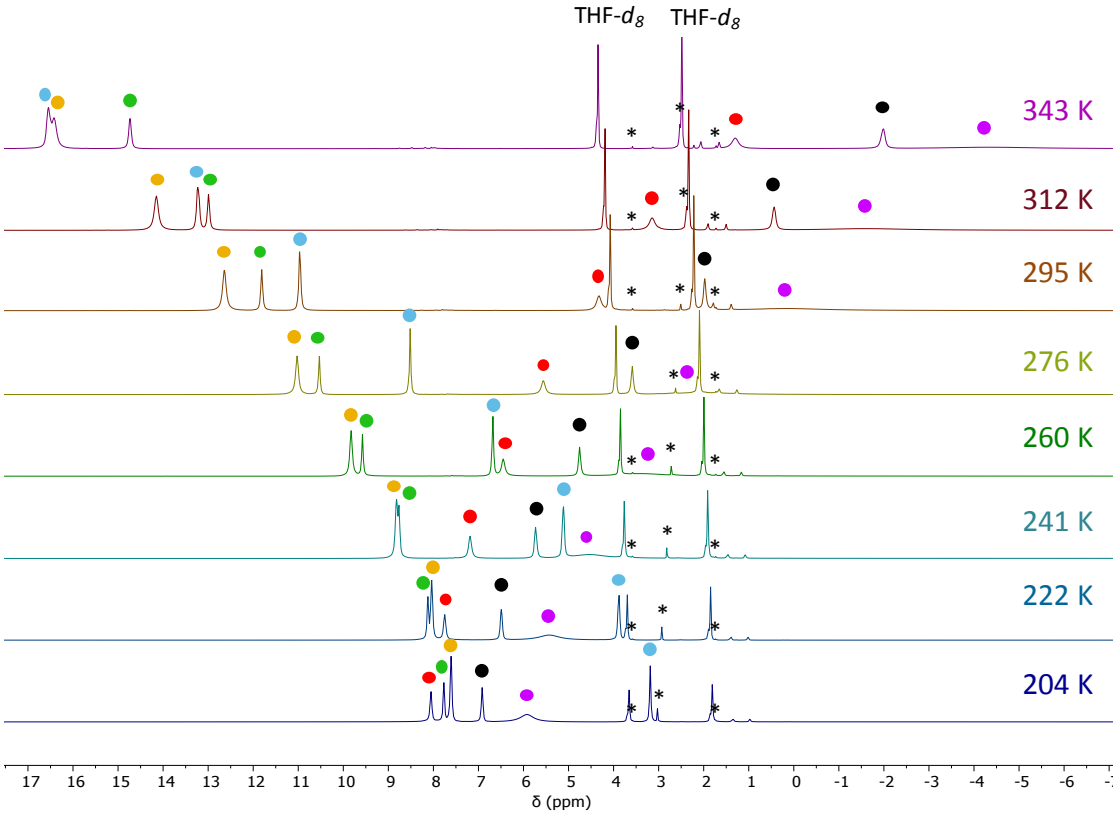

Figure S10. ^{1}H NMR spectra of **1** between 204K and 343 K (THF-d_8, 500 MHz).

VT-NMR analysis for Fe[(C_6H_4(p-F))NNC(p-Tol)NN(C_6H_4(p-F))]$_2$ (2)

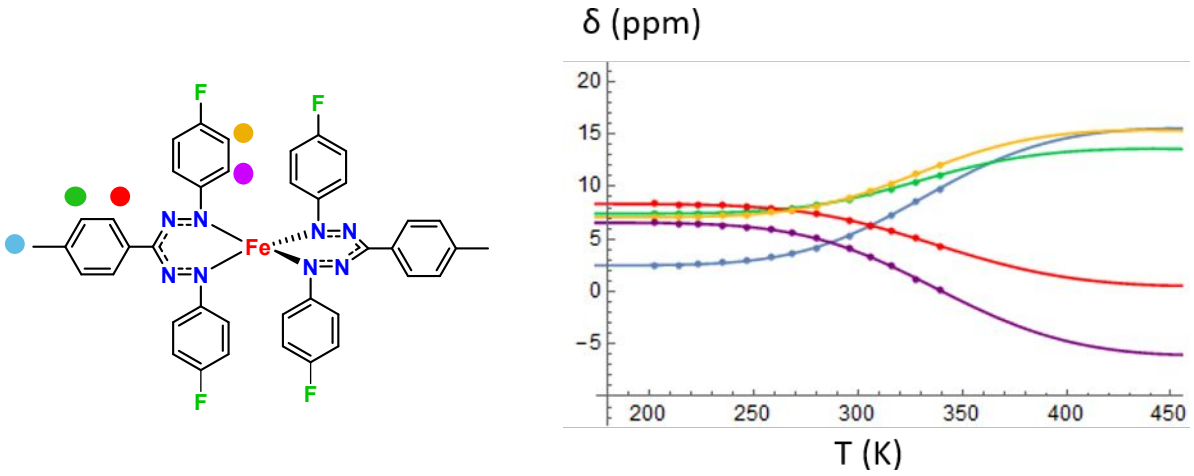

Figure S11. Temperature dependence of the ^{1}H NMR signals of **2** (THF-d_8 solution). Data fitted with the ideal solution model equation.

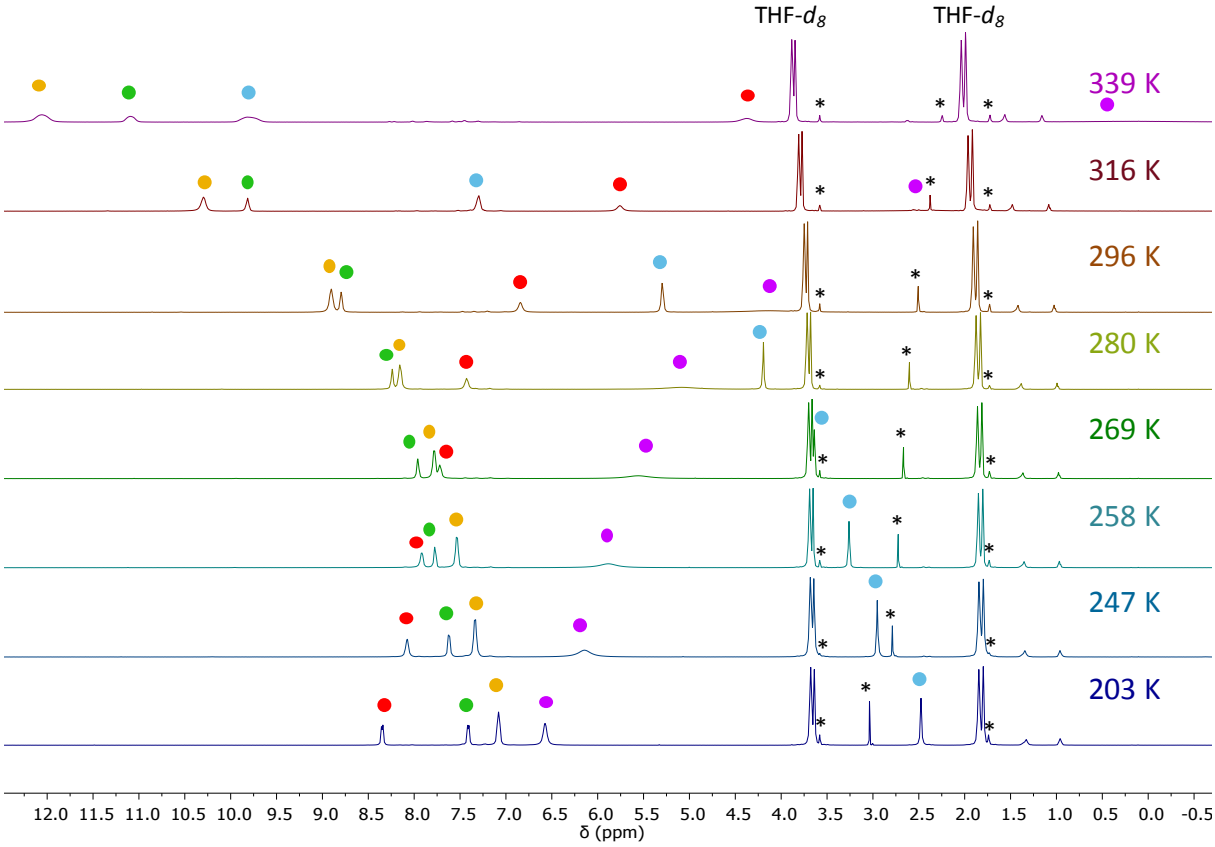

Figure S12. ^{1}H NMR spectra of **2** between 203K and 339 K (THF-d_8, 500 MHz).

VT-NMR analysis for Fe[(p-An)NNC(Ph)NN(p-An)]$_2$ (3)

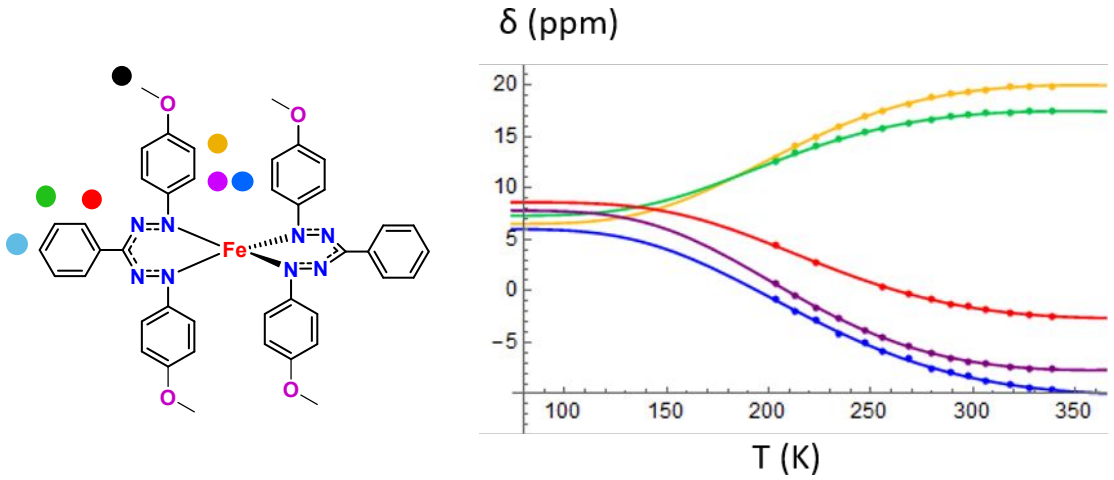

Figure S13. Temperature dependence of the ^{1}H NMR signals of **3** (THF-d_8 solution). Data fitted with the ideal solution model equation.

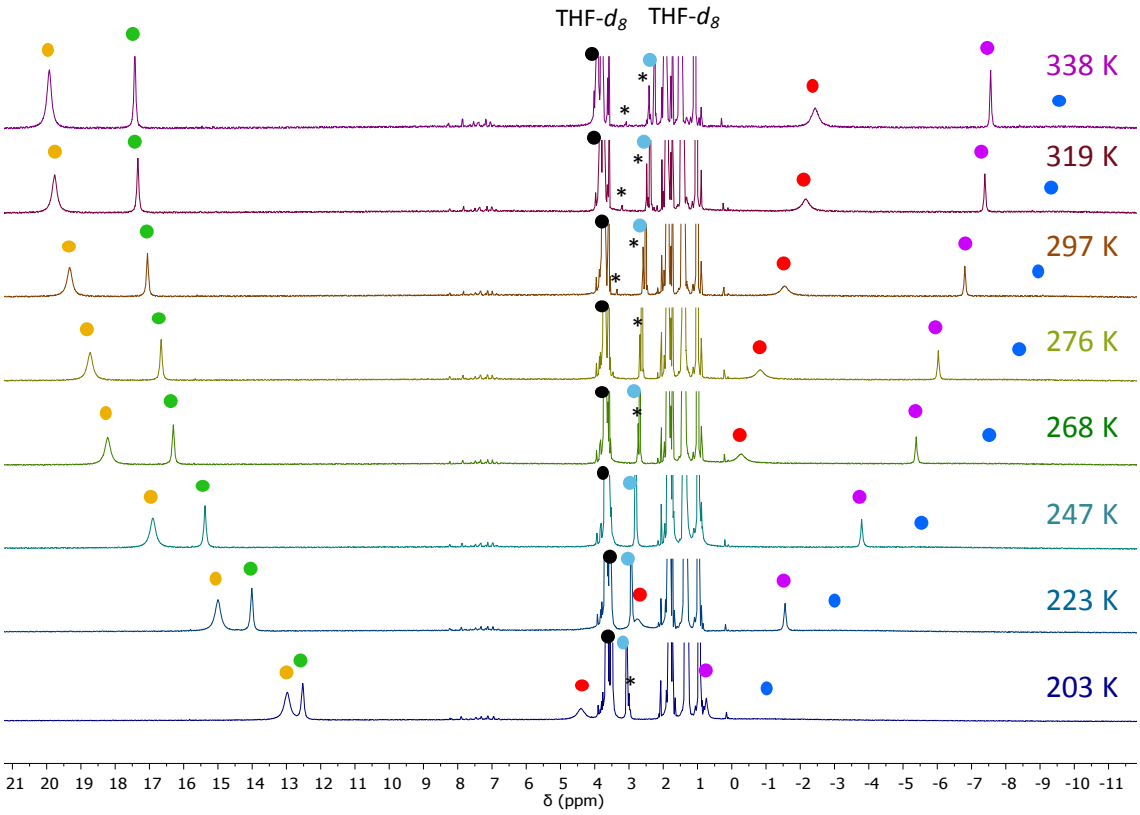

Figure S14. ^{1}H NMR spectra of **3** between 203 K and 338 K (THF-d_8, 500 MHz). Two inequivalent *o*-CH resonances of the *p*-An moiety are observed due to hindered rotation around the N-Ar bond.

VT-NMR analysis for Fe[PhNNC(C_6H_4(p-F))NNPh]$_2$ (4)

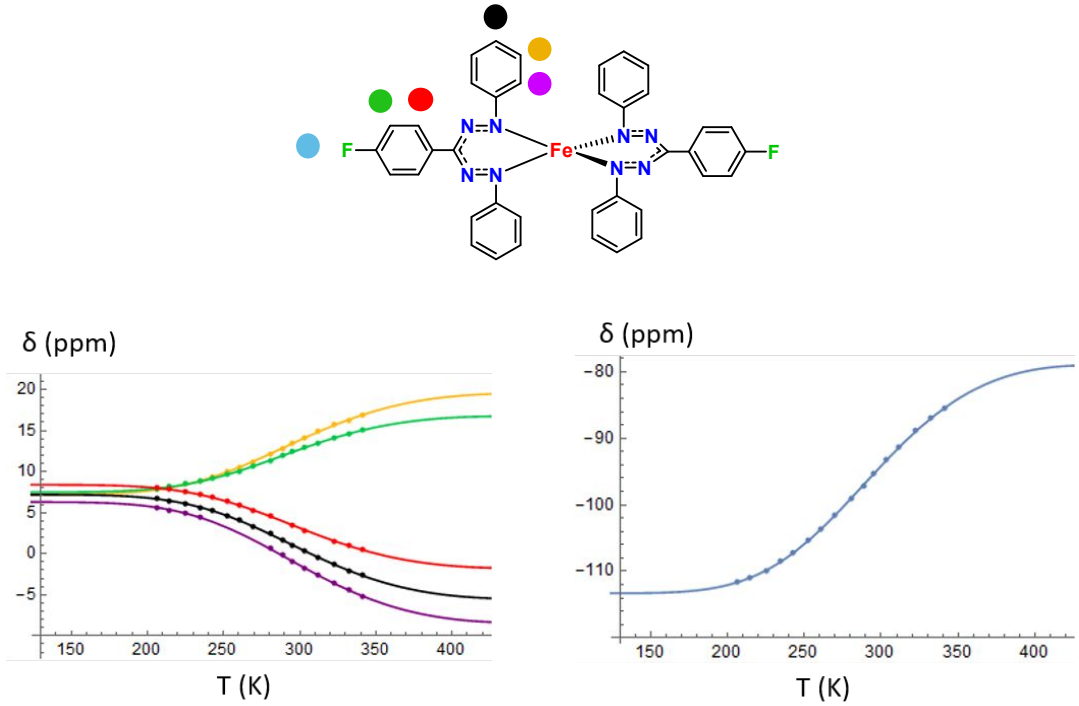

Figure S15. Temperature dependence of the ^{1}H NMR (left) and ^{19}F NMR signals (right) of **4** (THF-d_8 solution). Data fitted with the ideal solution model equation.

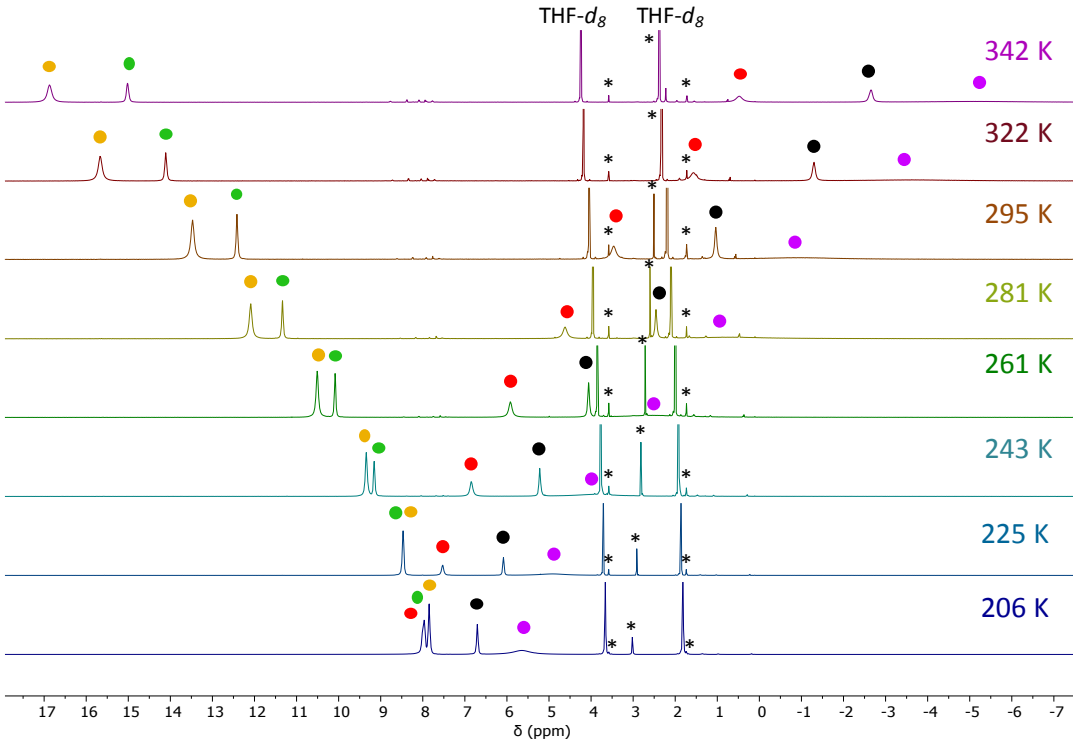

Figure S16. ^{1}H NMR spectra of **4** between 206 K and 342 K (THF-d_8, 500 MHz).

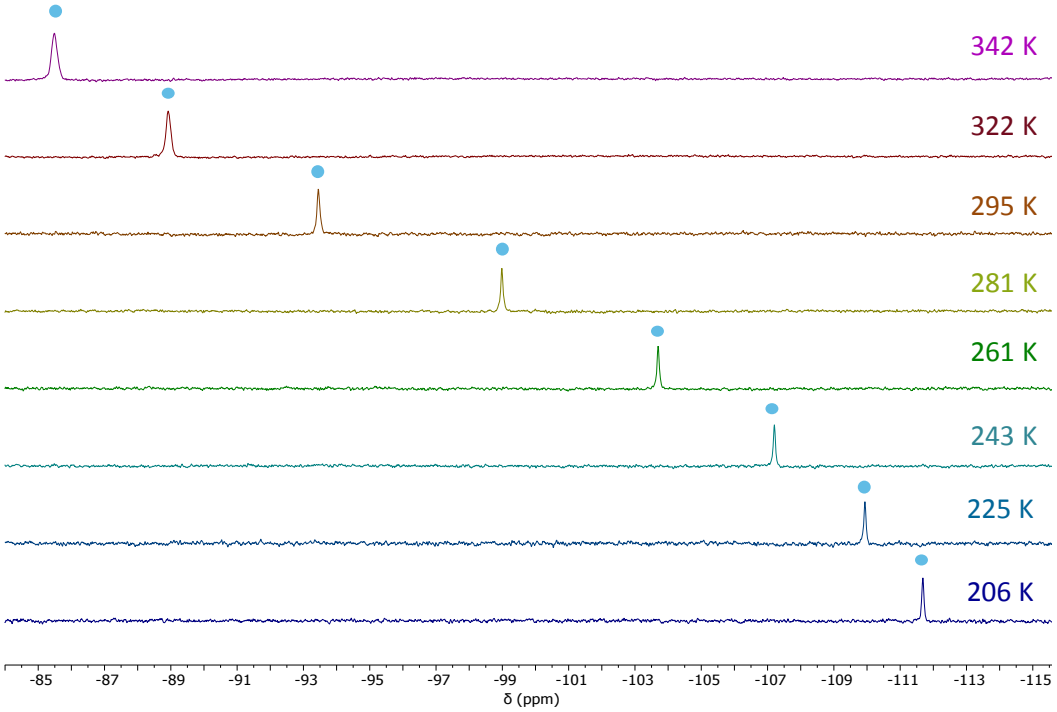

Figure S17. ^{19}F NMR spectra of **4** between 206 K and 342 K (THF-d_8, 470 MHz).

VT-NMR analysis Fe[PhNNC(p-An)NNPh]$_2$ (5)

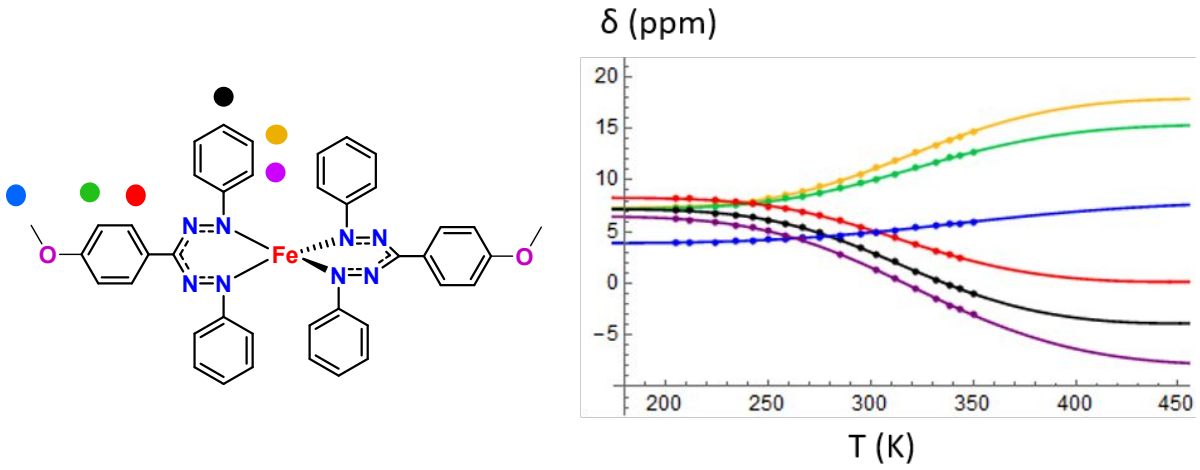

Figure S18. Temperature dependence of the ^{1}H NMR signals of **5** (THF-d_8 solution). Data fitted with the ideal solution model equation.

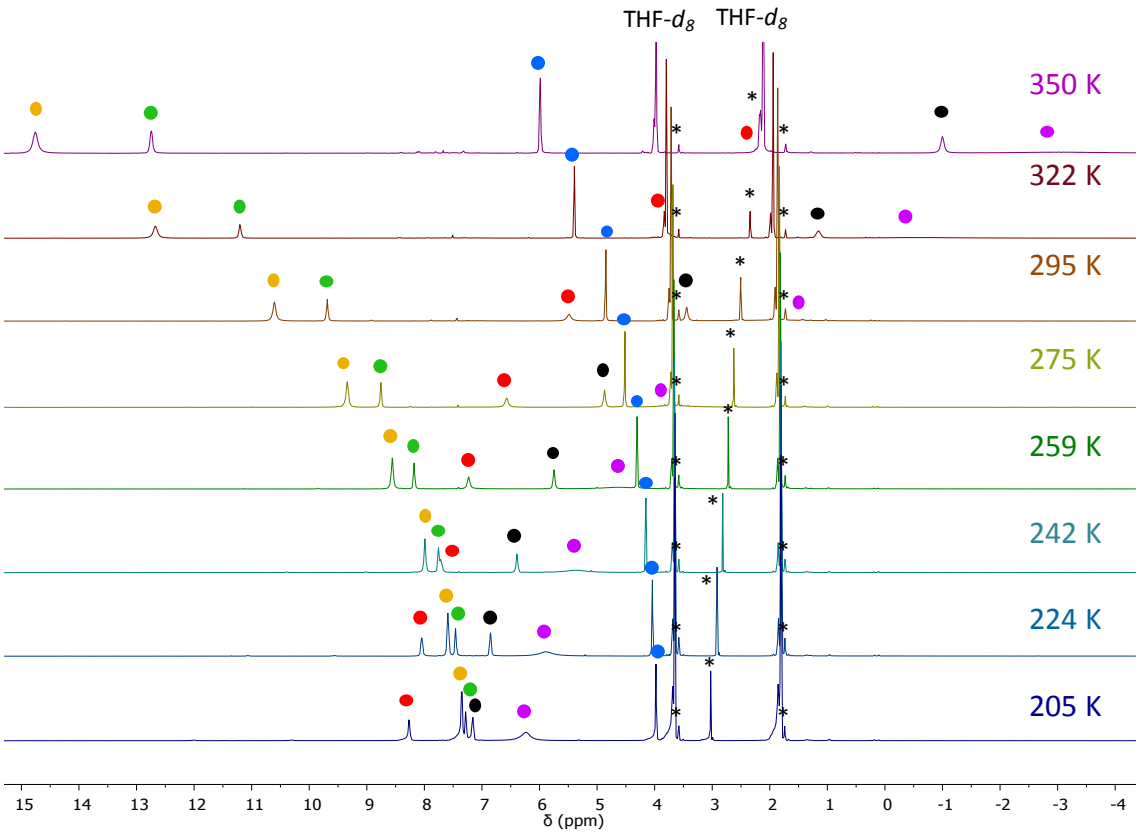

Figure S19. ^{1}H NMR spectra of **5** between 205 K and 350 K (THF-d_8, 500 MHz).

VT-NMR analysis for Fe[PhNNC(Ph)NNPh]$_2$ (6)

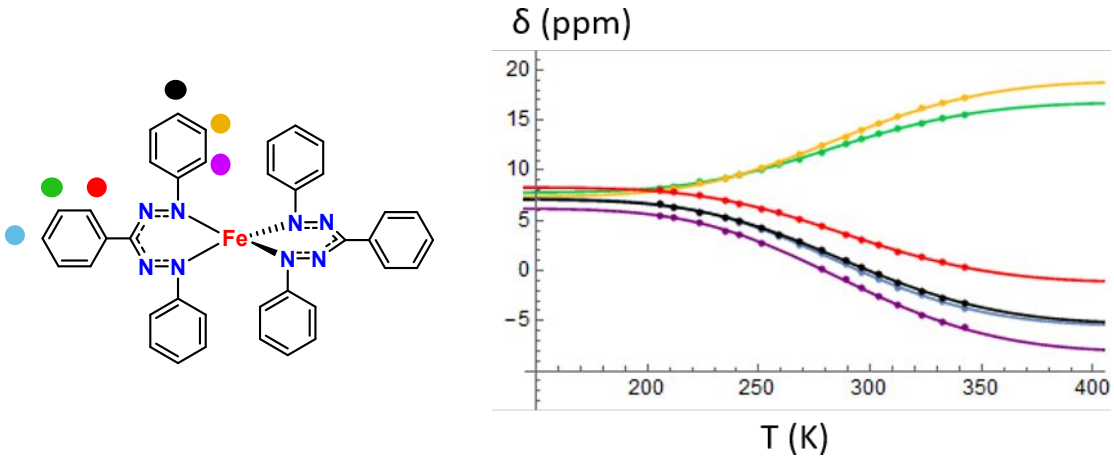

Figure S20. Temperature dependence of the ^{1}H NMR signals of **6** (THF-d_8 solution). Data fitted with the ideal solution model equation.

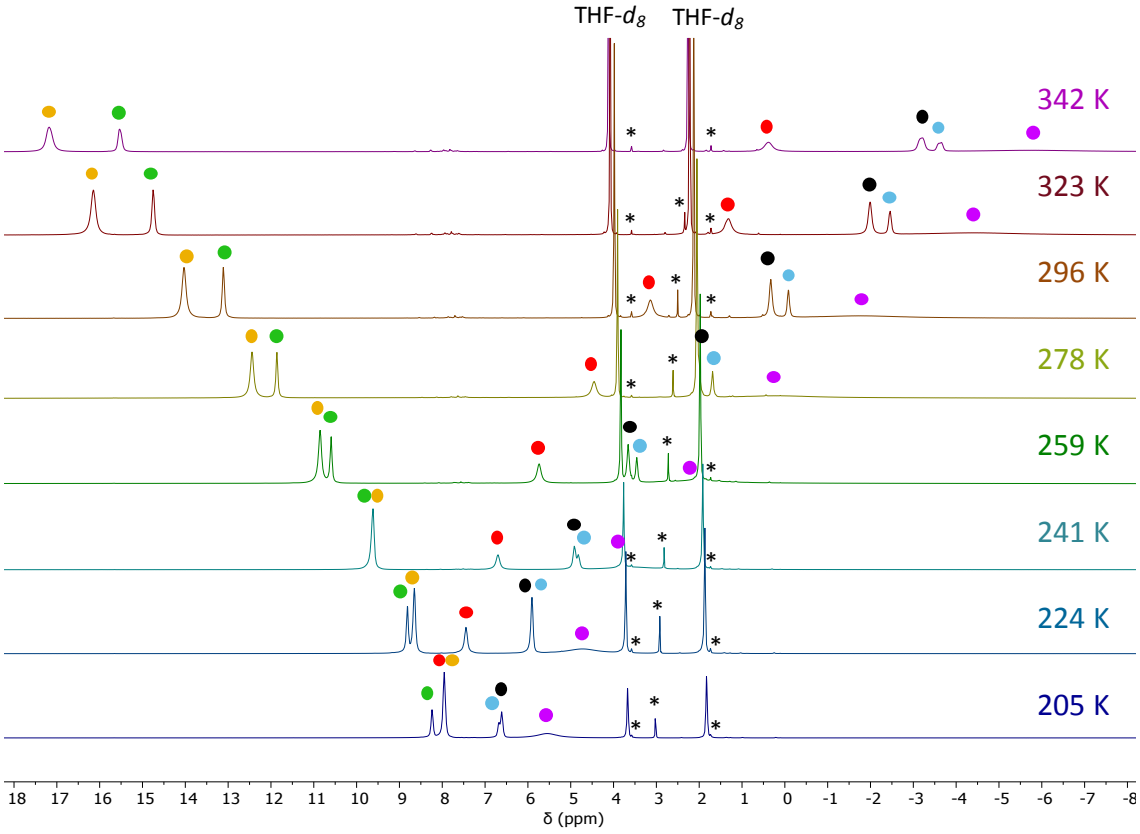

Figure S21. ^{1}H NMR spectra of **6** between 205 K and 342 K (THF-d_8, 500 MHz).

Magnetic measurements in solution

The mass susceptibility was determined using eq S8,[16] which is an approximation of eq S9:[17]

(eq S8) $$\chi_m \approx \frac{-3\Delta f}{4\pi f m}$$

(eq S9) $$\chi_m = \frac{-3\Delta f}{4\pi f m} + \chi_0 + \frac{\chi_0(d_0 - d_s)}{m}$$

where:
χ_m ≈ mass susceptibility of the solute (cm^3/g)
Δf ≈ observed frequency shift of reference resonance (Hz)
f ≈ spectrometer frequency (Hz)
χ_0 ≈ mass susceptibility of solvent (cm^3/g)
m ≈ mass of substance per cm^3 of solution (g/cm^3)
d_0 ≈ density of solvent (g/cm^3)
d_s ≈ density of solution (g/cm^3)

The mass susceptibility (χ_m) was corrected for the (atomic) diamagnetic contributions using Pascal's constants.[18] The temperature dependence of the density of the solvent was taken into account as described in Section ” Analysis of temperature dependence of the magnetic susceptibility and of the molar extinction coefficient” (see above).

Table S6. Effective magnetic moment (μ_{eff}) and magnetic susceptibility as a function of temperature (χT) for compounds **1-6** measured by Evans method in THF-d_8.

	ΔT (K)	μ_{eff} (μ_B)	χT ($cm^3 \cdot K \cdot mol^{-1}$)
1	204 – 343	1.2 – 4.1	0.17 – 2.08
2[a]	203 – 339	1.3 – 3.1	0.20 – 1.24
3	208 – 334	2.7 – 4.4	0.92 – 2.41
4	212 – 345	1.7 – 3.8	0.35 – 1.82
5[a]	205 – 350	1.4 – 3.7	0.23 – 1.84
6	205 – 342	1.4 – 4.1	0.24 – 2.08

[a] Crystals of **2** and **5** contain respectively 0.75 and 0.5 THF per iron complex.

UV-Vis data and analysis of temperature dependence of molar extinction coefficient

The temperature dependent UV-vis spectra were recorded in a THF or toluene solution (~10^{-5} M) using an Agilent Cary 8454 UV/Vis spectrophotometer equipped with a CoolSpek USP-203 cryostat using quartz cuvettes with screw cap which was sealed under nitrogen in a glovebox.

Table S7. Selected peak wavelengths, λ_{max} (nm), for the low-spin state (173 K) and high-spin state (from scaled subtraction of the data at 293 and 173 K) for compounds **1-6** in THF.

	λ_{max} (nm) for LS	λ_{max} (nm) for HS
1	360, 406, 533	470, 580
2	365, 405, 535	402, 449, 576
3	427, 544	314, 475, 586
4	357, 405, 529	463, 573
5	413, 540	486, 593
6	350, 405, 525	465, 572

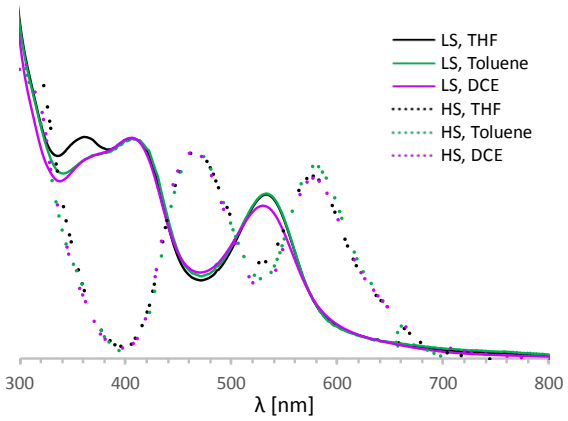

Figure S22. Comparison of (normalized) spectral data of **1** for the low-spin state (183 K for THF and toluene and 143 K for 1,2-dichloroethane) and high-spin state (from scaled subtraction of the data at 293 and 143 K).

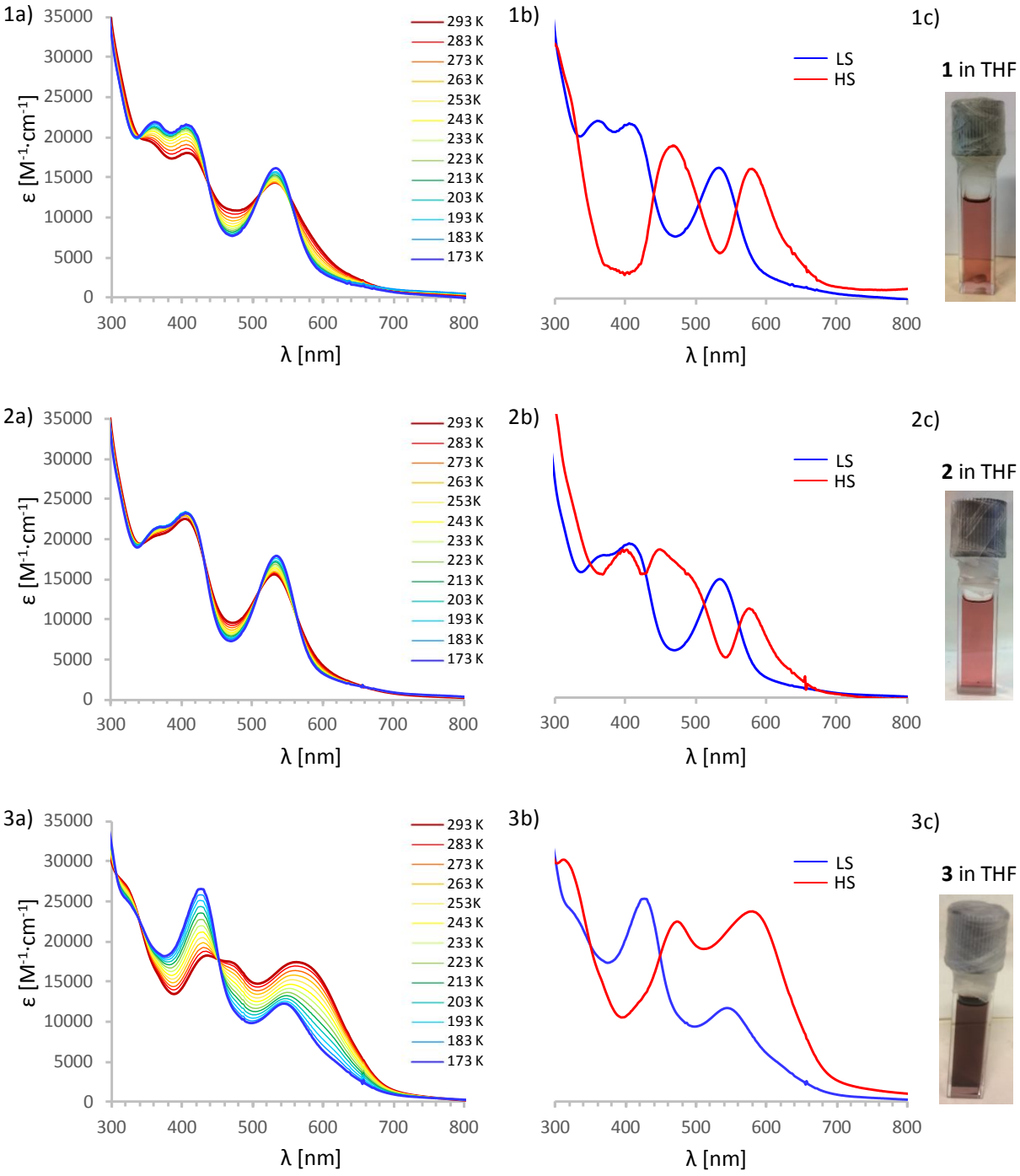
1a)
ε [M-1·cm-1]
λ [nm]
293 K
283 K
273 K
263 K
253K
243 K
233 K
223 K
213 K
203 K
193 K
183 K
173 K
1b)
LS
HS
λ [nm]
1c)
1 in THF
2a)
ε [M-1·cm-1]
λ [nm]
2b)
LS
HS
λ [nm]
2c)
2 in THF
3a)
ε [M-1·cm-1]
λ [nm]
3b)
LS
HS
λ [nm]
3c)
3 in THF

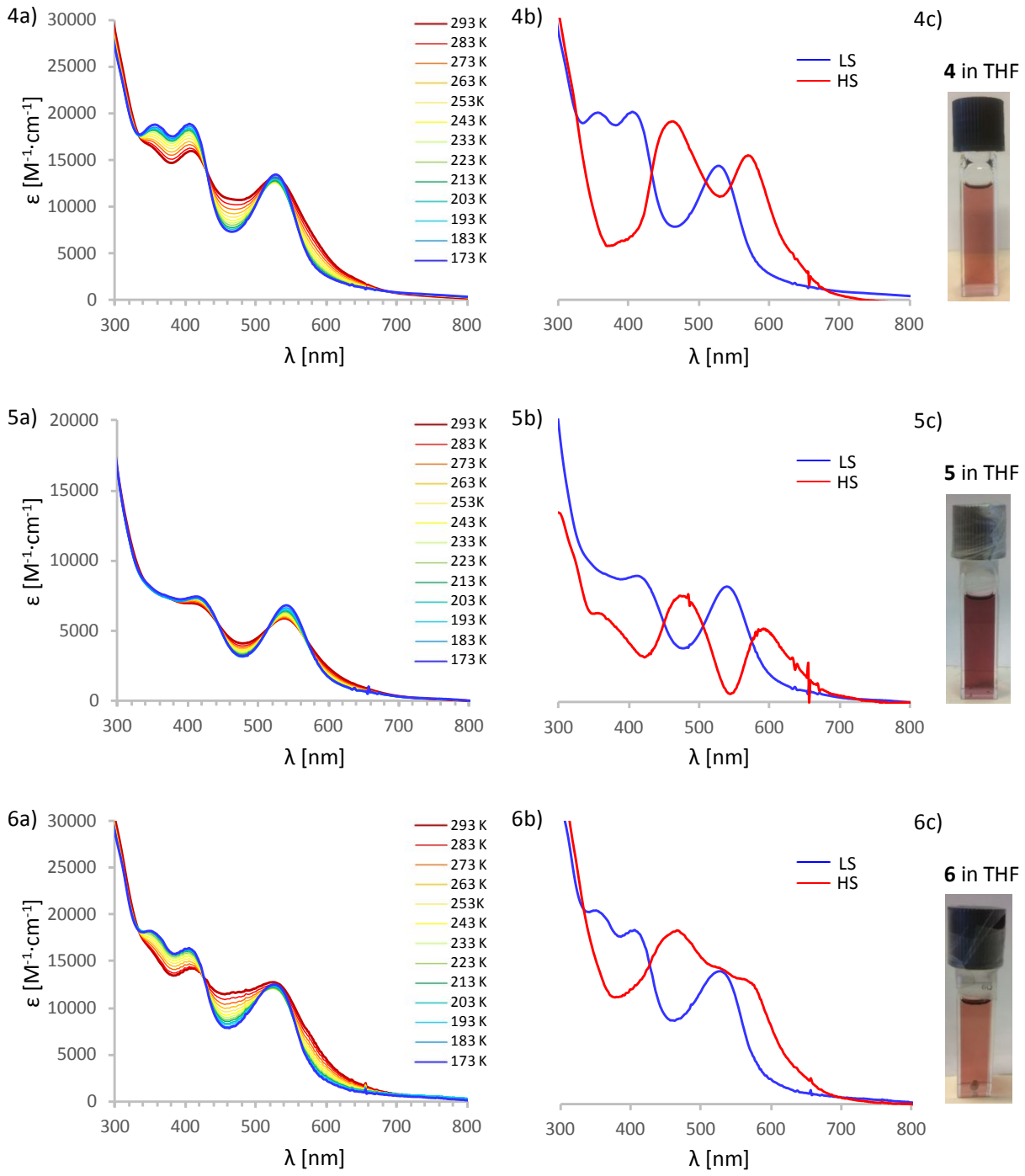

Figure S23. a) Variable-temperature UV-Vis spectra of **1-6** between 173–293 K in THF (**1**: $c = 3.79 \cdot 10^{-5}$ M, **2**: $c = 3.90 \cdot 10^{-5}$ M, **3**: $c = 4.84 \cdot 10^{-5}$ M, **4**: $c = 4.64 \cdot 10^{-5}$ M, **5**: $c = 4.23 \cdot 10^{-5}$ M, **6**: $c = 4.95 \cdot 10^{-5}$ M at r.t), b) comparison of (normalized) spectral data for the low-spin state (173 K) and high-spin state (from scaled subtraction of the data at 293 and 173 K), c) Physical appearance of the THF solution of compounds **2-6**.

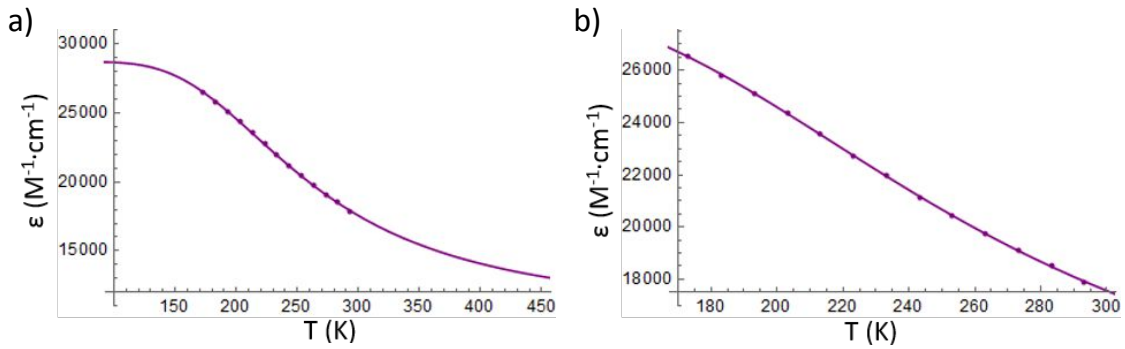

Figure S24. Plot of the molar extinction coefficient ε vs. T at 426 nm for **3**. The solid line represents the calculated curve fit.

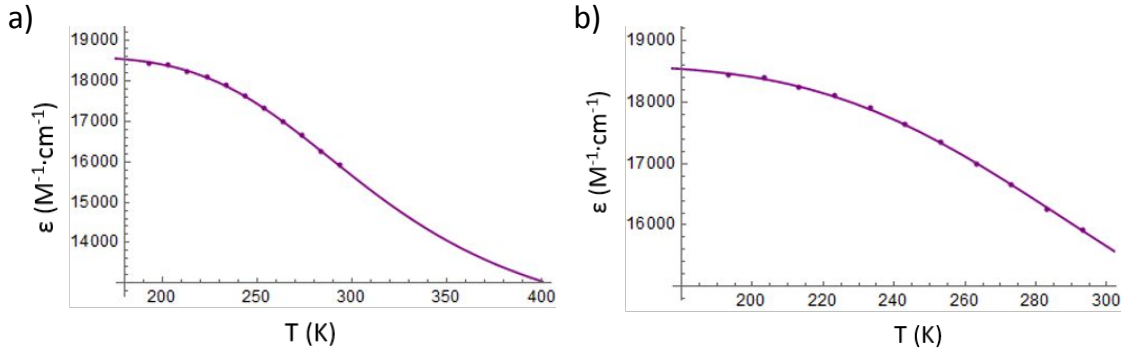

Figure S25. Plot of the molar extinction coefficient ε vs. T at 405 nm for **4**. The solid line represents the calculated curve fit.

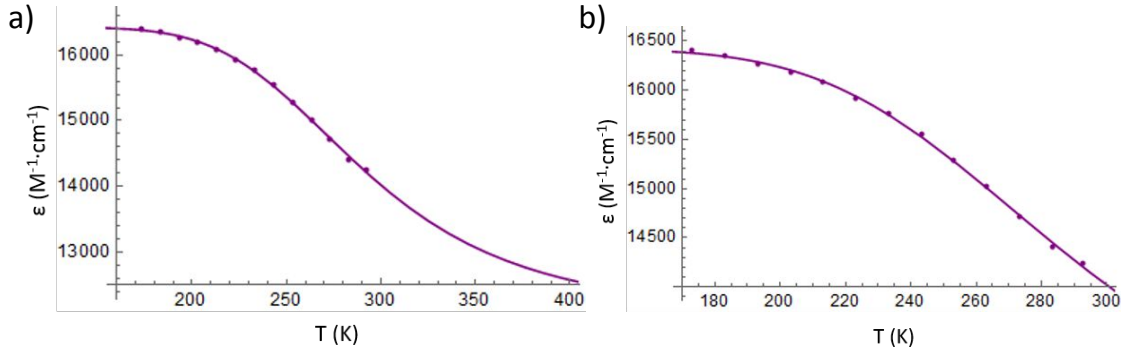

Figure S26. Plot of the molar extinction coefficient ε vs. T at 405 nm for **6**. The solid line represents the calculated curve fit.

Analysis of temperature dependence of γ_{HS}

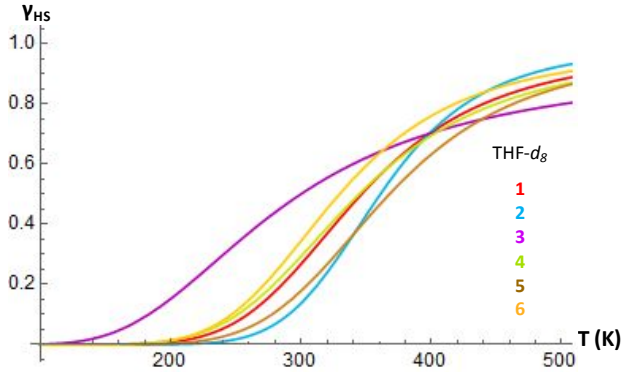

Figure S27. Temperature dependence of the high-spin fraction (γ_{HS}) of compounds **1-6** in THF-d_8 calculated from the temperature dependence of the chemical shift (δ).

Table S8. Fitted parameter for compounds **2-6**R for the different sets of empirical data: NMR chemical shifts (δ), solution magnetic susceptibilities (χ) and molar extinction coefficients (ε) from UV-Vis spectra, as described in Section *"Analysis of the thermodynamic parameters for the spin crossover equilibrium"*.

	ΔH (kJ·mol^{-1})	ΔS (J·mol^{-1}·K^{-1})	Selected λ (nm)	ε_{LS} (M^{-1}·cm^{-1})	ε_{HS} (M^{-1}·cm^{-1})
2(δ)	27.2 ± 0.5	75 ± 2			
2(χ)	25.5 ± 0.4	71 ± 1			
3(δ)	8.6 ± 0.2	29 ± 1			
3(ε)	8.0 ± 0.5	29 ± 3	426	28733 ± 230	9055 ± 1173
4(δ)	16.9 ± 0.3	49 ± 2			
4(χ)	16.1 ± 0.3	49 ± 1			
4(ε)	15.7 ± 0.1	49[a]	405	18623 ± 21	11210 ± 274
5(δ)	20.6 ± 0.1	56 ± 1			
5(χ)	21.9 ± 1.0	60 ± 3			
6(δ)	17.9 ± 0.1	54 ± 1			
6(χ)	18.6 ± 0.4	60 ± 1			
6(ε)	16.8 ± 1.0	58 ± 7	405	16416 ± 28	12180 ± 597

[a] the ΔS value was fixed to the value derived from the fitting of the chemical shift.

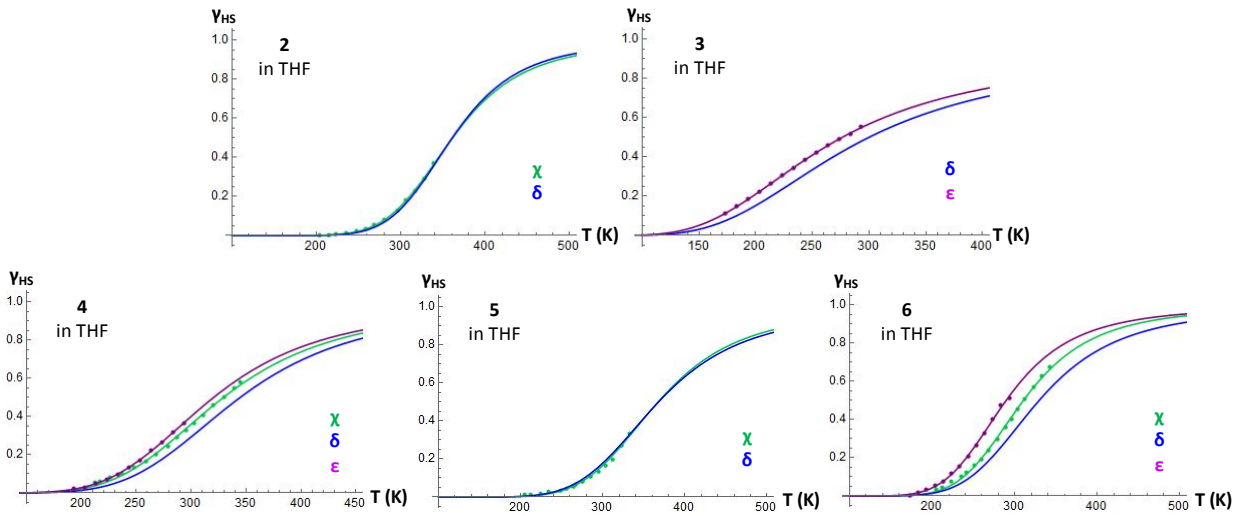

Figure S28. Plot of the mole fraction of **2-6** in the HS state (γ_{HS}) vs. T. The solid line represents the simulation using fit parameters described in the text.

NMR characterization

Note: Asterisks (*) in the NMR spectra indicate the residual resonances of THF-d_8 and a small amount of water in the sealed capillary, which as inserted in the NMR tube to obtain the temperature-dependence of the solution magnetic moment (Evans method).

NMR spectra for Fe[(C$_6$H$_4$(p-F))NNC(p-Tol)NN(C$_6$H$_4$(p-F))]$_2$ (2)

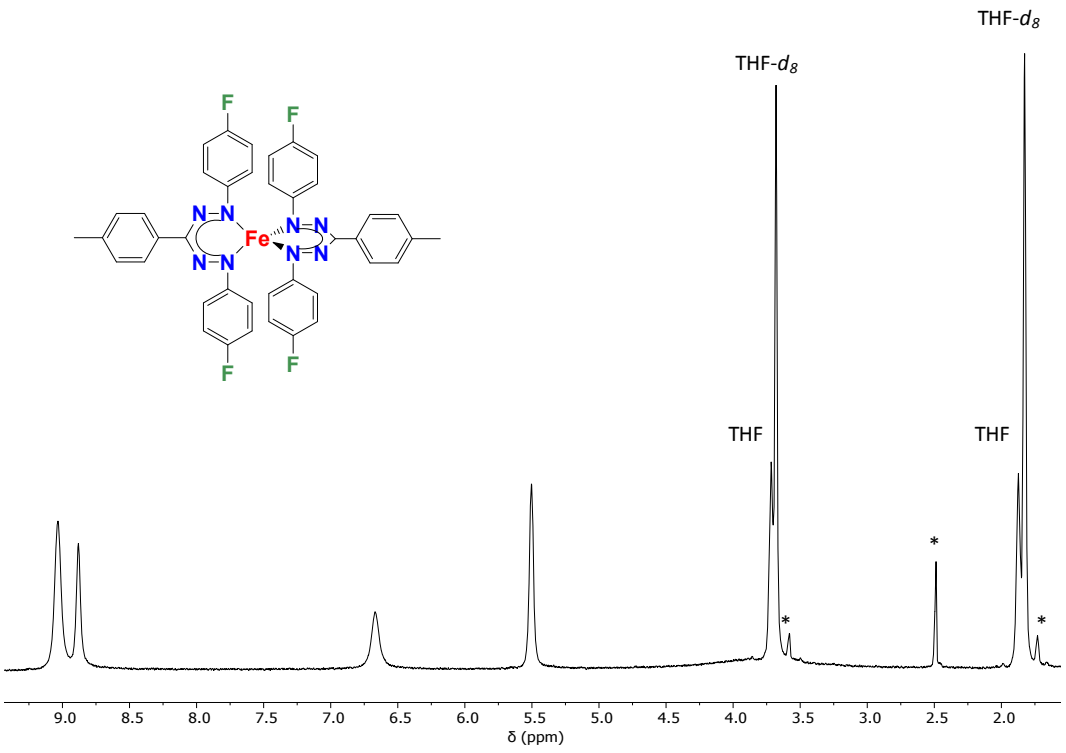

Figure S29. ^{1}H NMR spectrum of **2** (THF-d_8, 400 MHz, 25 °C).

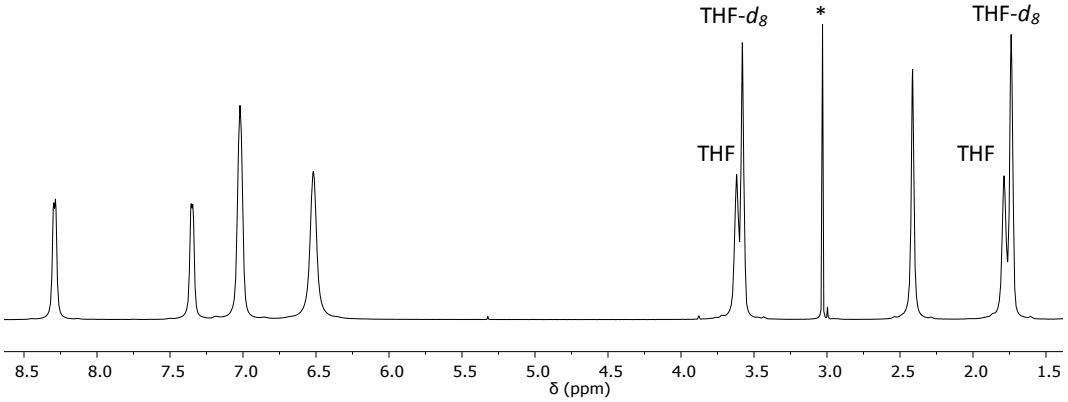

Figure S30. ^{1}H NMR spectrum of **2** (THF-d_8, 500 MHz, -70 °C).

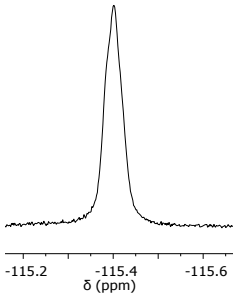

Figure S31. ^{19}F NMR spectrum of **2** (THF-d_8, 470 MHz, -70 °C).

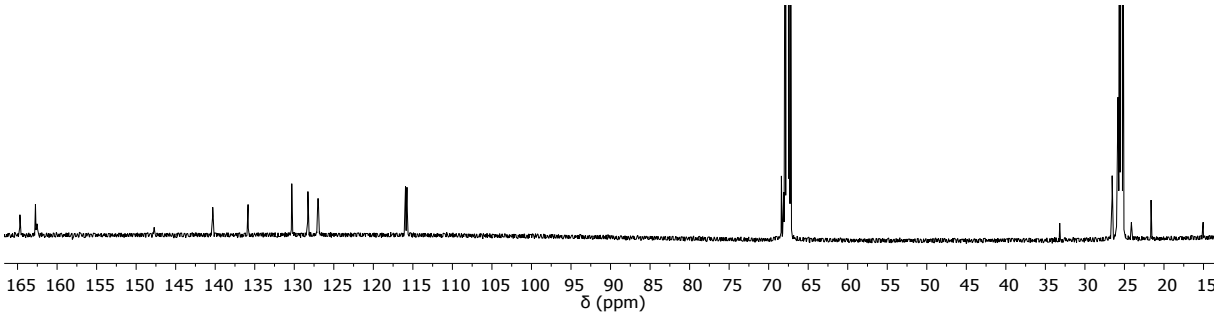

Figure S32. ^{13}C NMR spectrum of **2** (THF-d_8, 126 MHz, -70 °C).

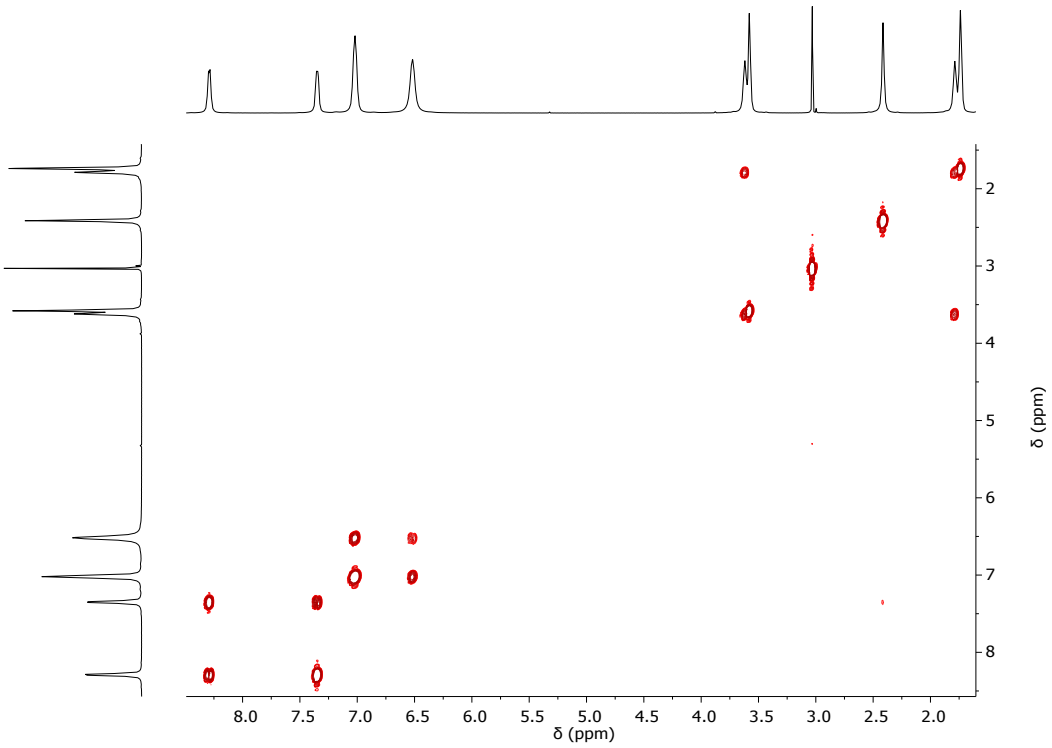

Figure S33. ^{1}H-^{1}H COSY spectrum of (THF-d_8, 500 MHz, -70 °C).

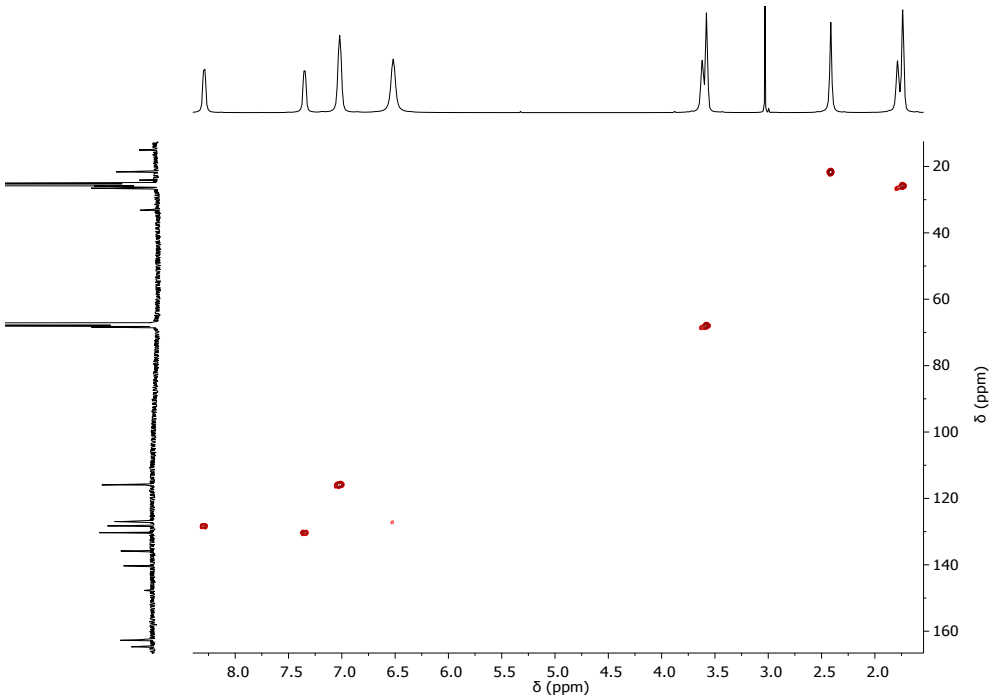

Figure S34. ^{1}H-^{13}C gHSQCAD spectrum of **2** (THF-d_8, 500 MHz, -70 °C).

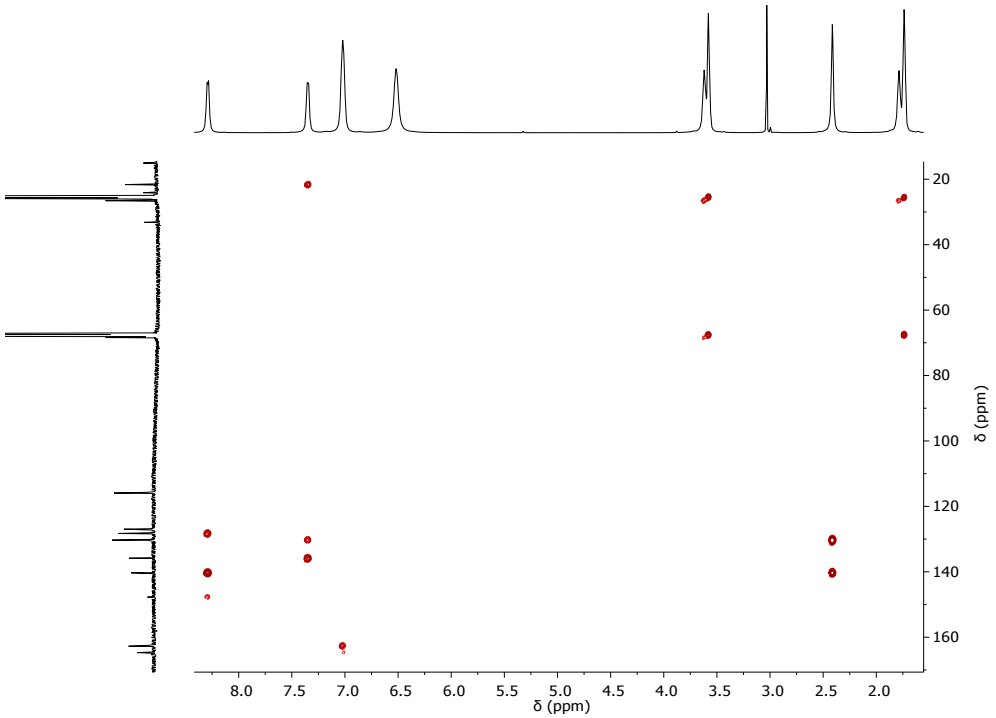

Figure S35. ^{1}H-^{13}C gHMBCAD spectrum of **2** (THF-d_8, 500 MHz, -70 °C).

NMR spectra for Fe[(p-An)NNC(Ph)NN(p-An)]$_2$ (3)

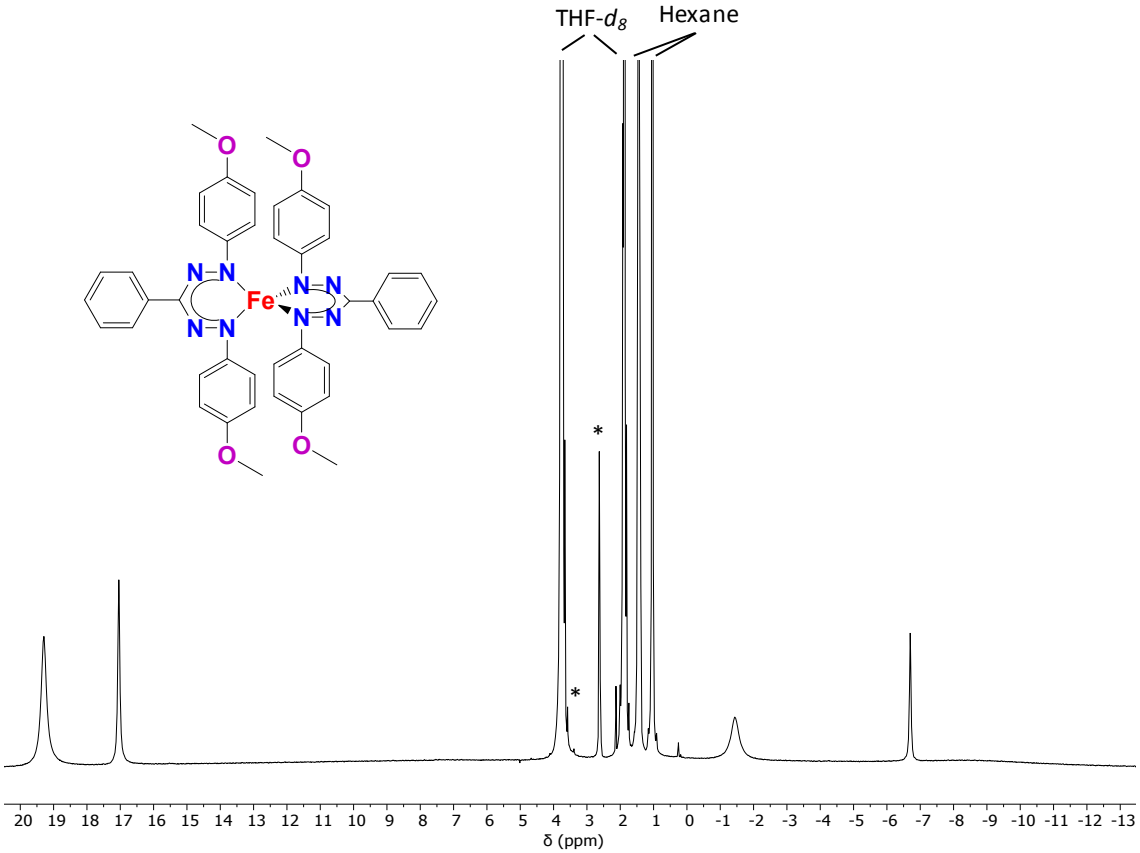

Figure S36. ^{1}H NMR spectrum of **3** (THF-d_8, 500 MHz, 25 °C).

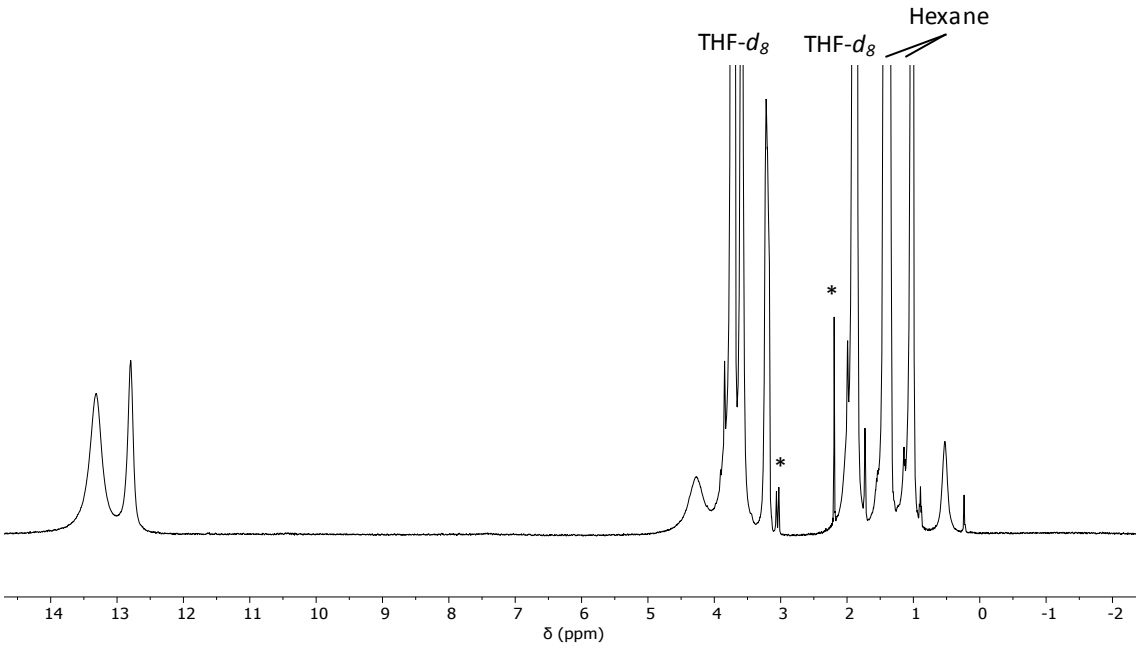

Figure S37. ^{1}H NMR spectrum of **3** (THF-d_8, 500 MHz, -70 °C).

NMR spectra for Fe[PhNNC(C_6H_4(p-F))NNPh]$_2$ (4)

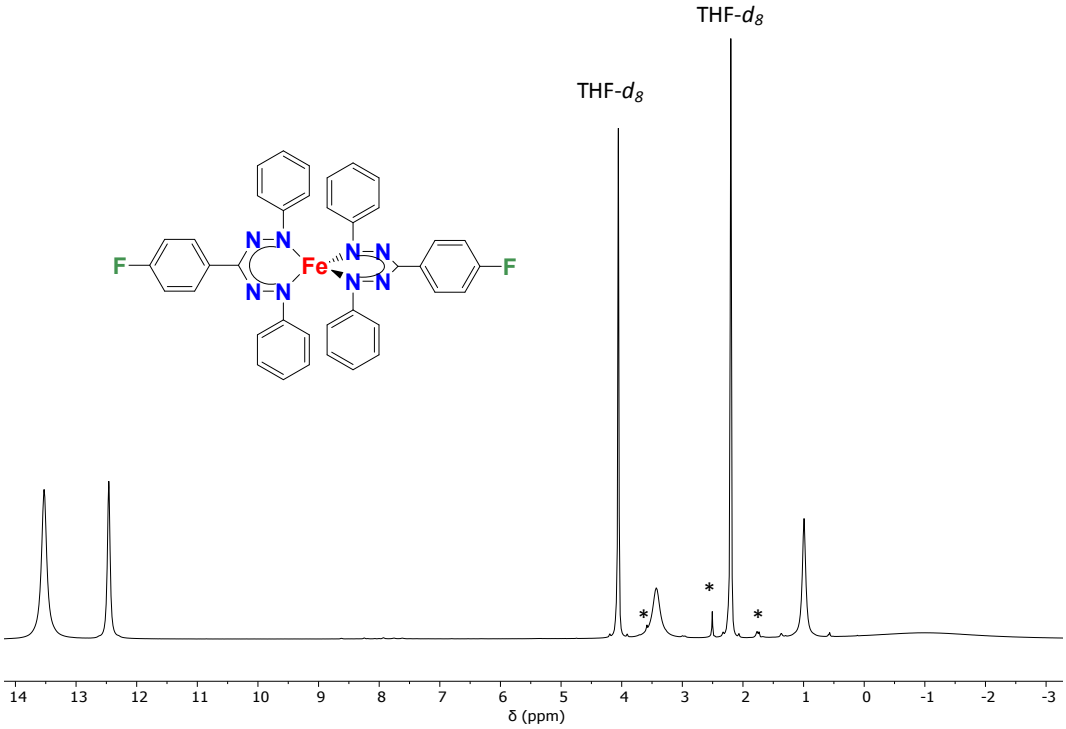

Figure S38. ^{1}H NMR spectrum of **4** (THF-d_8, 500 MHz, 25 °C).

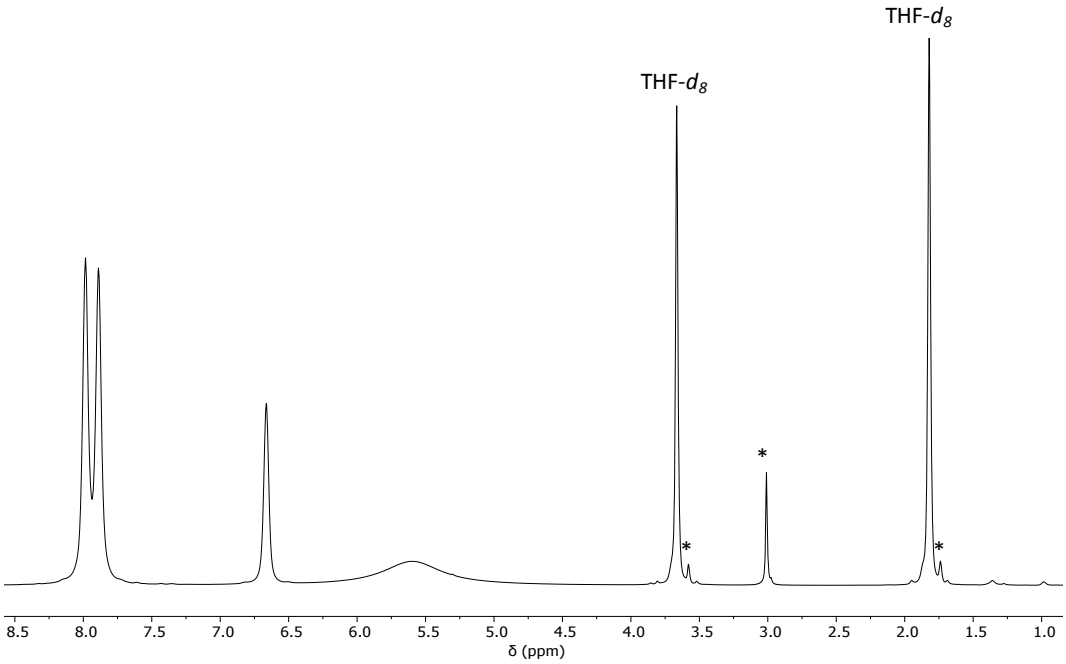

Figure S39. ^{1}H NMR spectrum of **4** (THF-d_8, 500 MHz, -65 °C).

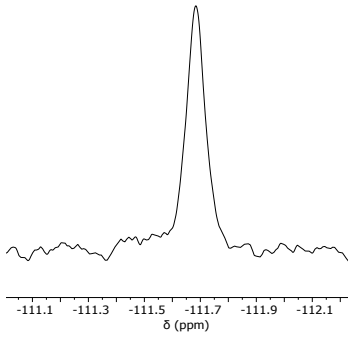

Figure S40. ^{19}F NMR spectrum of **4** (THF-d_8, 470 MHz, -65 °C).

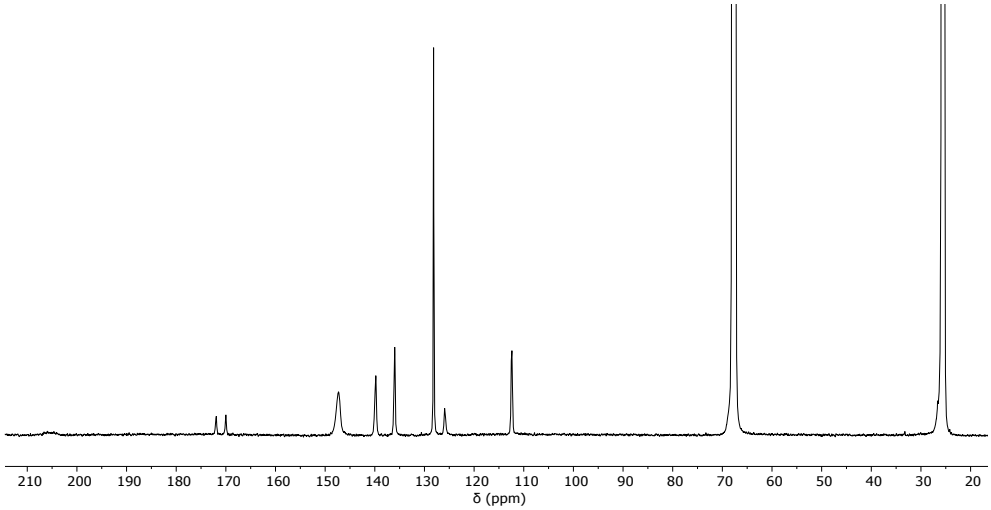

Figure S41. ^{13}C NMR spectrum of **4** (THF-d_8, 126 MHz, -65 °C).

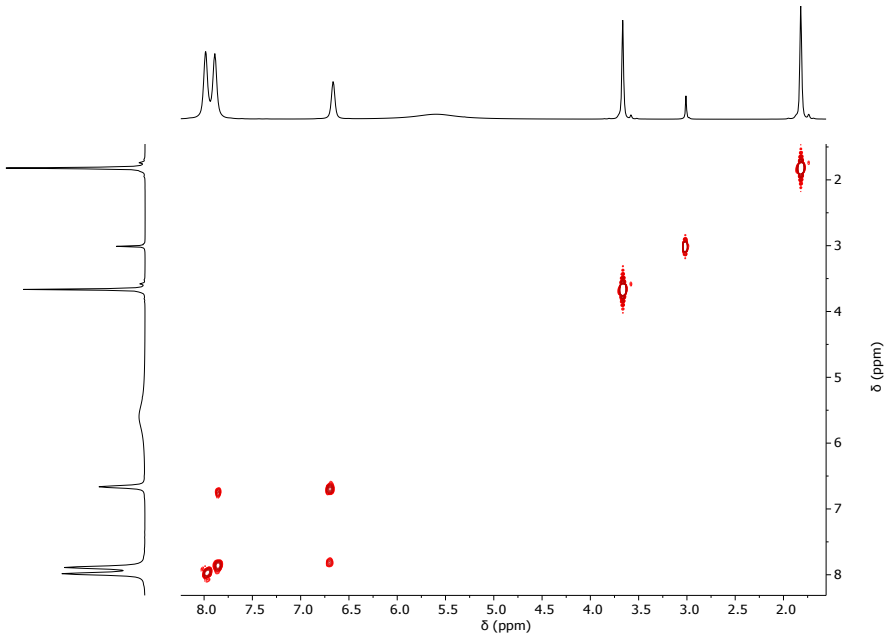

Figure S42. ^{1}H-^{1}H COSY spectrum of **4** (THF-d_8, 500 MHz, -65 °C).

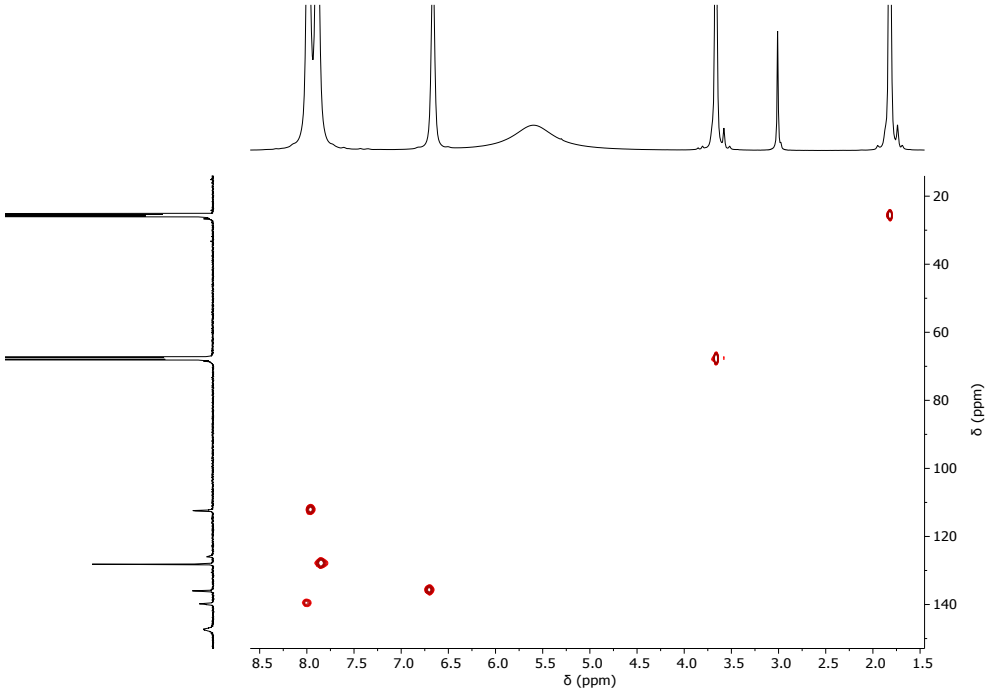

Figure S43. ^{1}H-^{13}C HSQC spectrum of **4** (THF-d_8, 500 MHz, -65 °C).

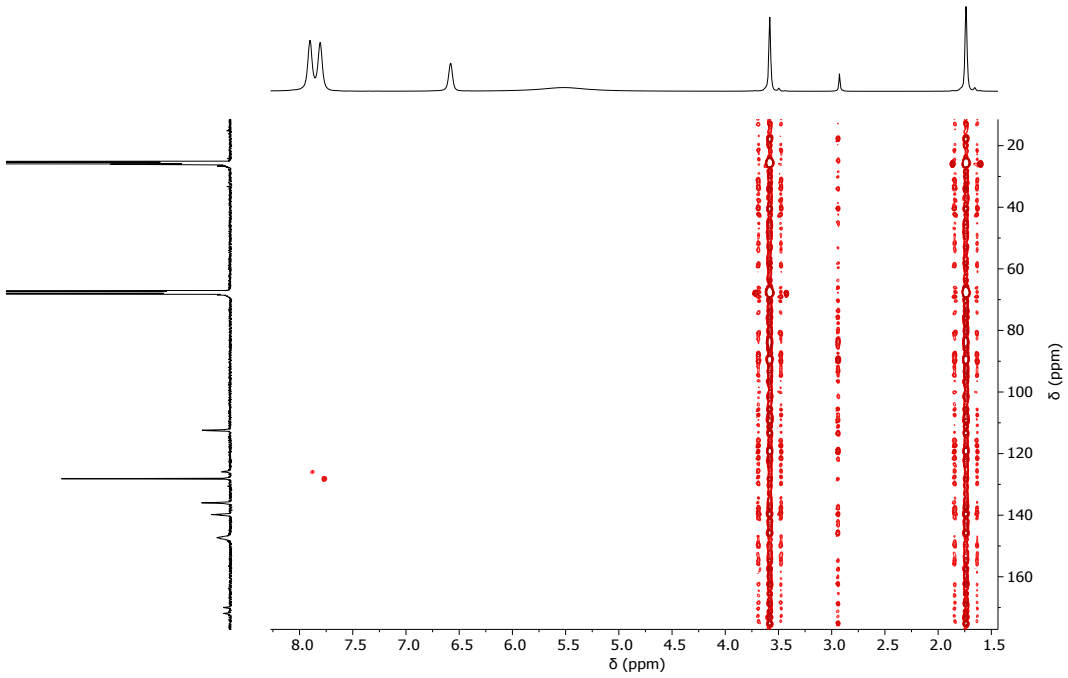

Figure S44. ^{1}H-^{13}C HMBC spectrum of **4** (THF-d_8, 500 MHz, -65 °C).

NMR spectra for Fe[PhNNC(p-An)NNPh]$_2$ (5)

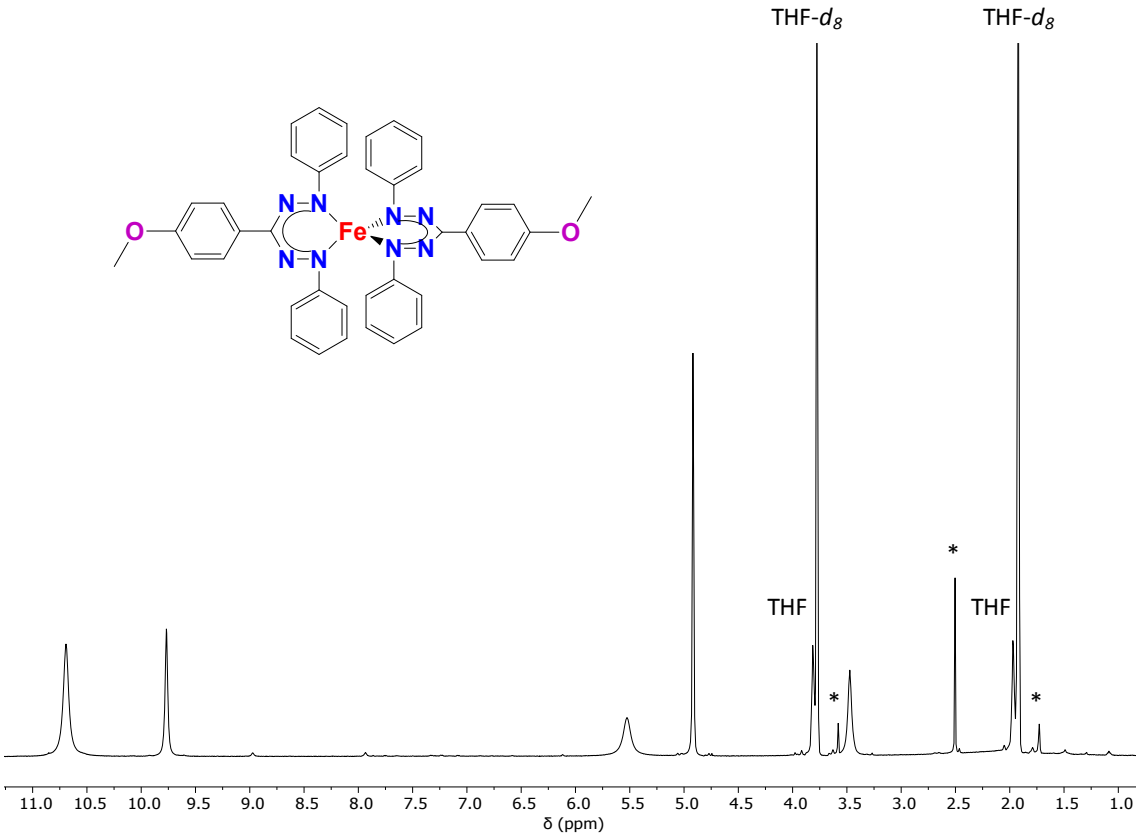

Figure S45. ^{1}H NMR spectrum of **5** (THF-d_8, 500 MHz, 25 °C).

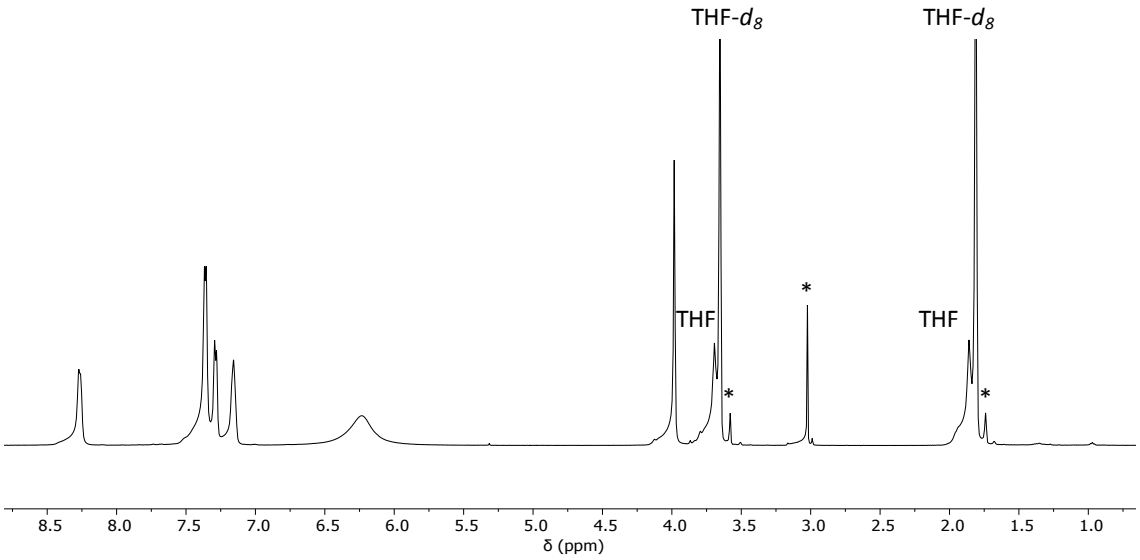

Figure S46. ^{1}H NMR spectrum of **5** (THF-d_8, 500 MHz, -70 °C).

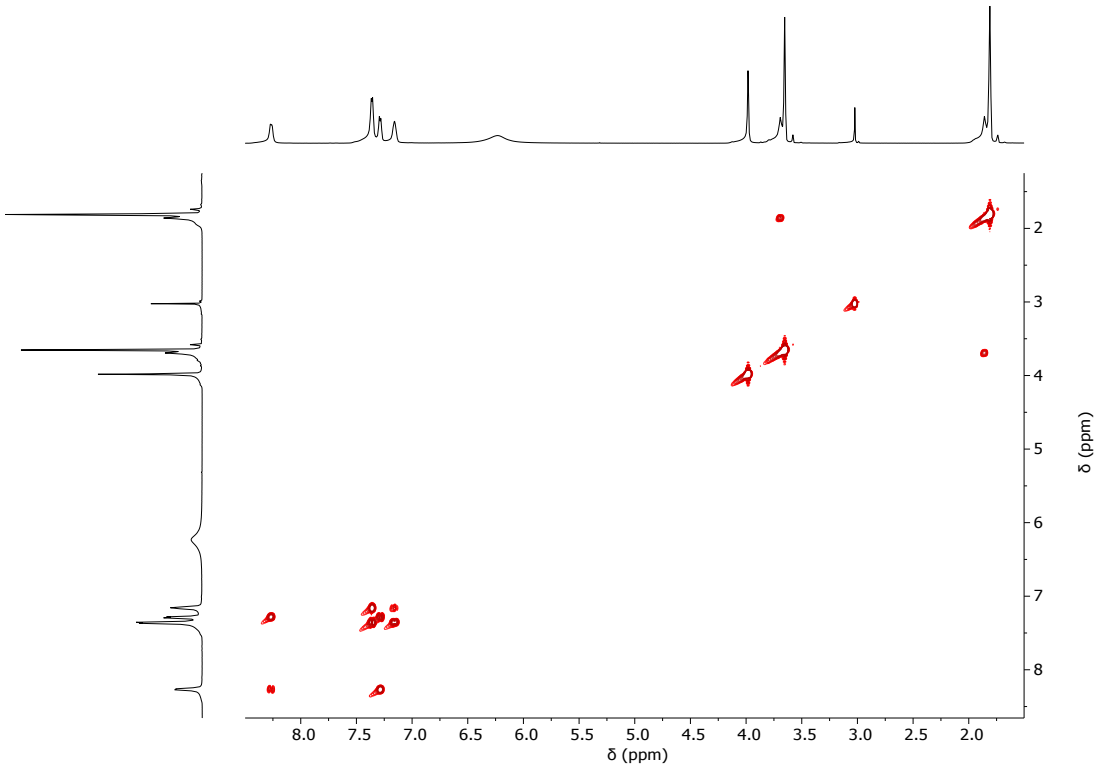

Figure S47. ^{1}H-^{1}H gCOSY spectrum of **5** (THF-d_8, 500 MHz, -70 °C).

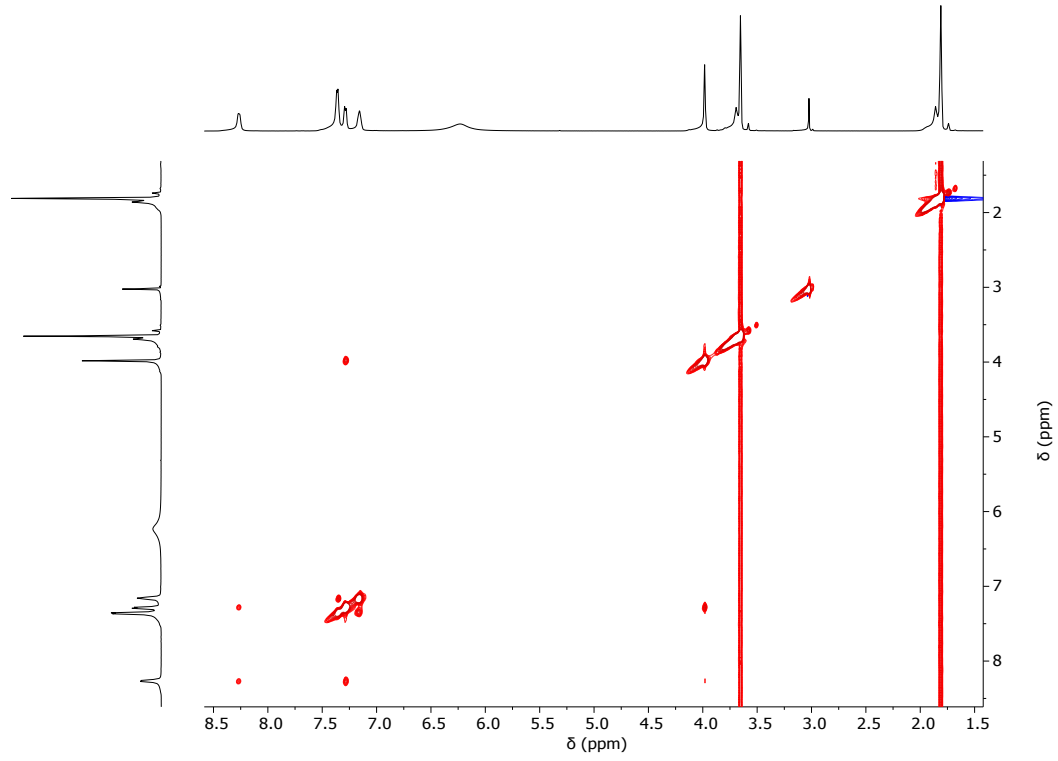

Figure S48. ^{1}H-^{1}H gNOESY spectrum of **5** (THF-d_8, 500 MHz, -70 °C).

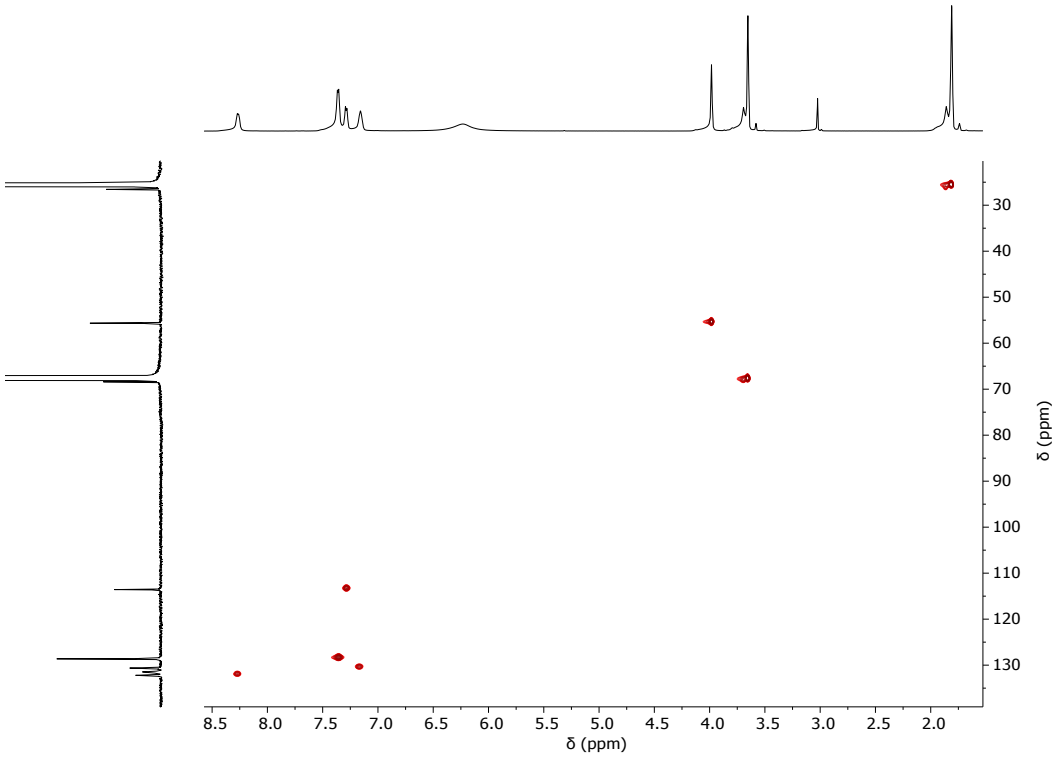

Figure S49. ^{1}H-^{13}C HMQC spectrum of **5** (THF-d_8, 500 MHz, -70 °C).

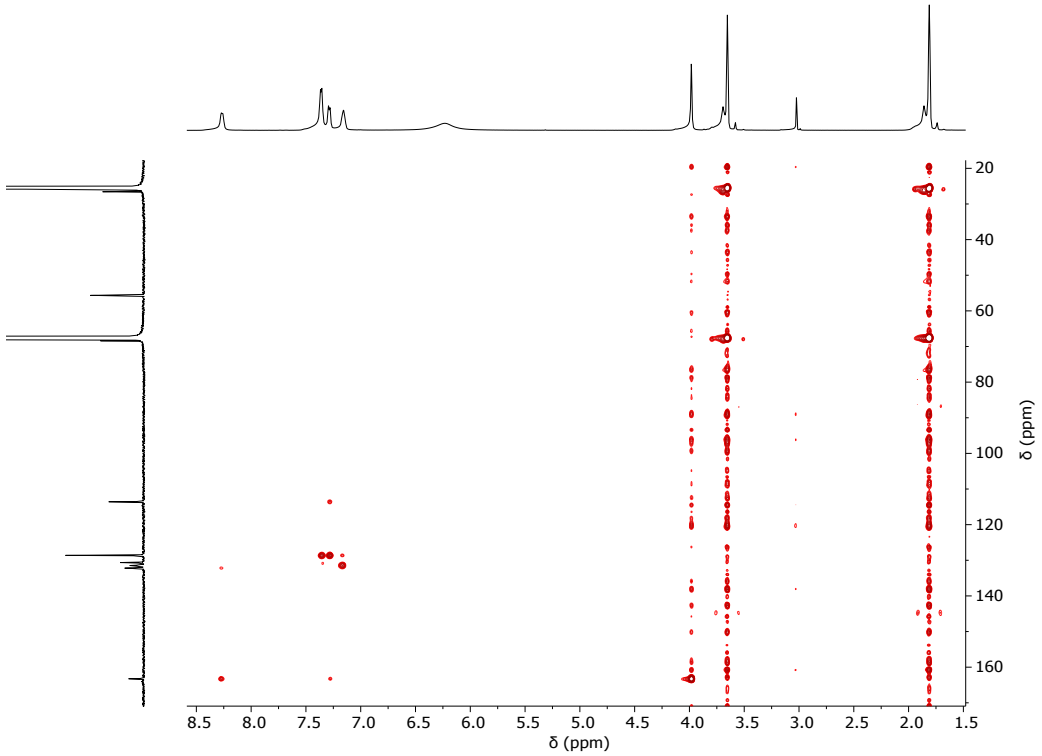

Figure S50. ^{1}H-^{13}C HMBC spectrum of **5** (THF-d_8, 500 MHz, -70 °C).

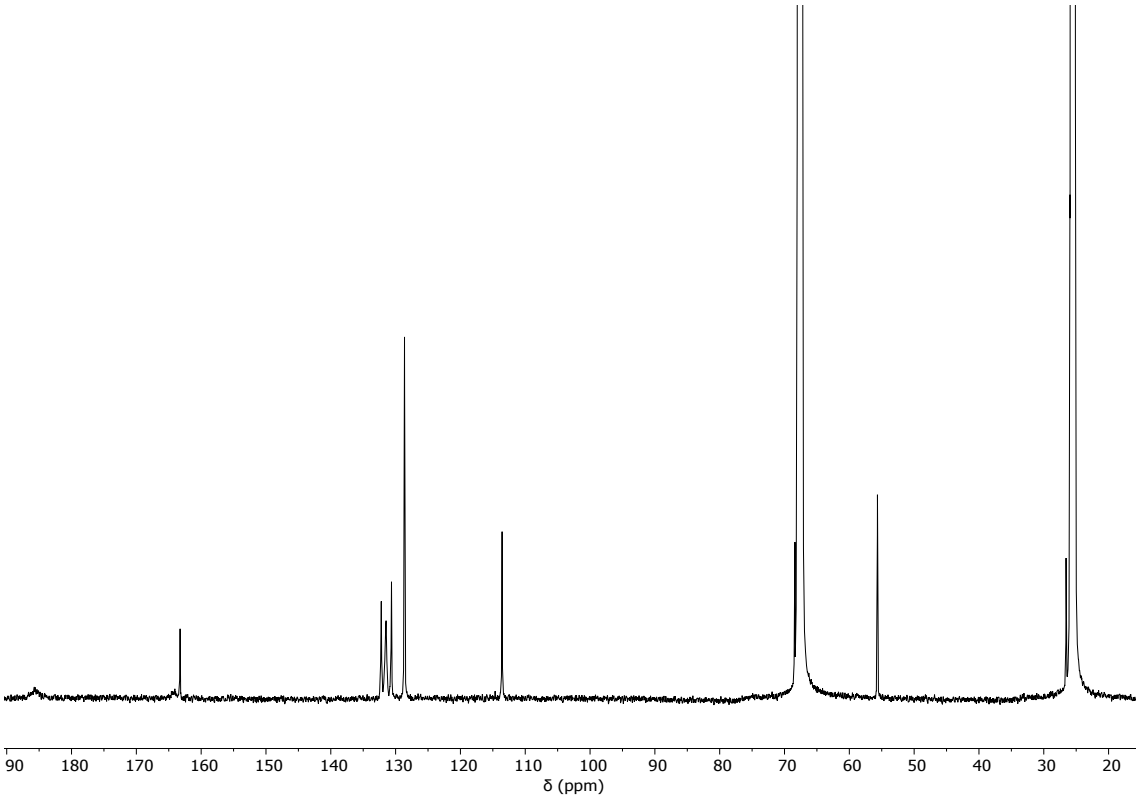

Figure S51. ^{13}C NMR spectrum of **5** (THF-d_8, 126 MHz, -70 °C).

NMR spectra for Fe[PhNNC(Ph)NNPh]$_2$ (6)

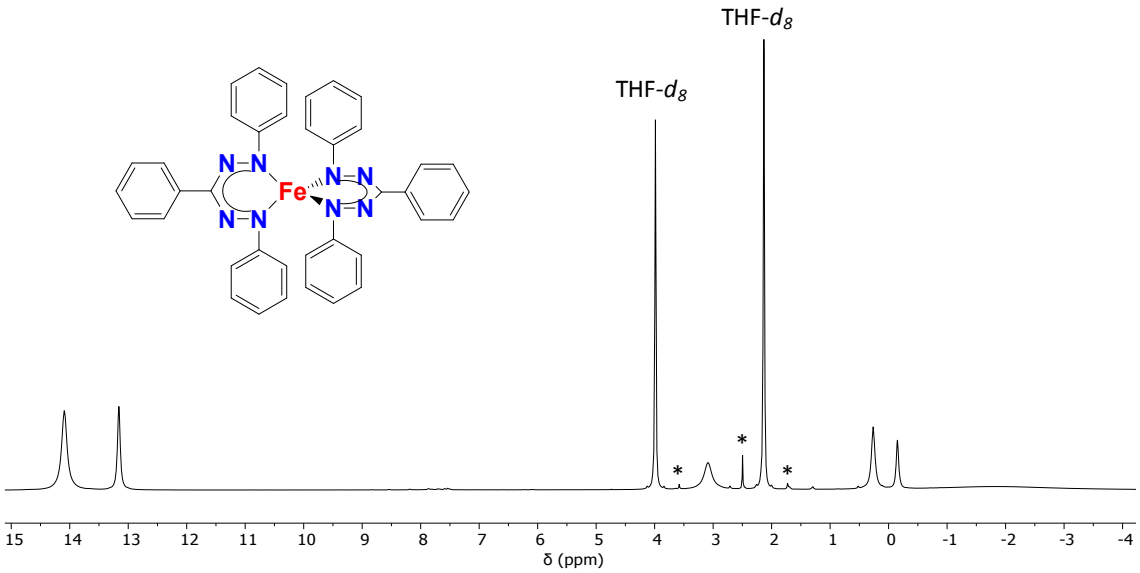

Figure S52. ^{1}H NMR spectrum of **6** (THF-d_8, 500 MHz, 25 °C).

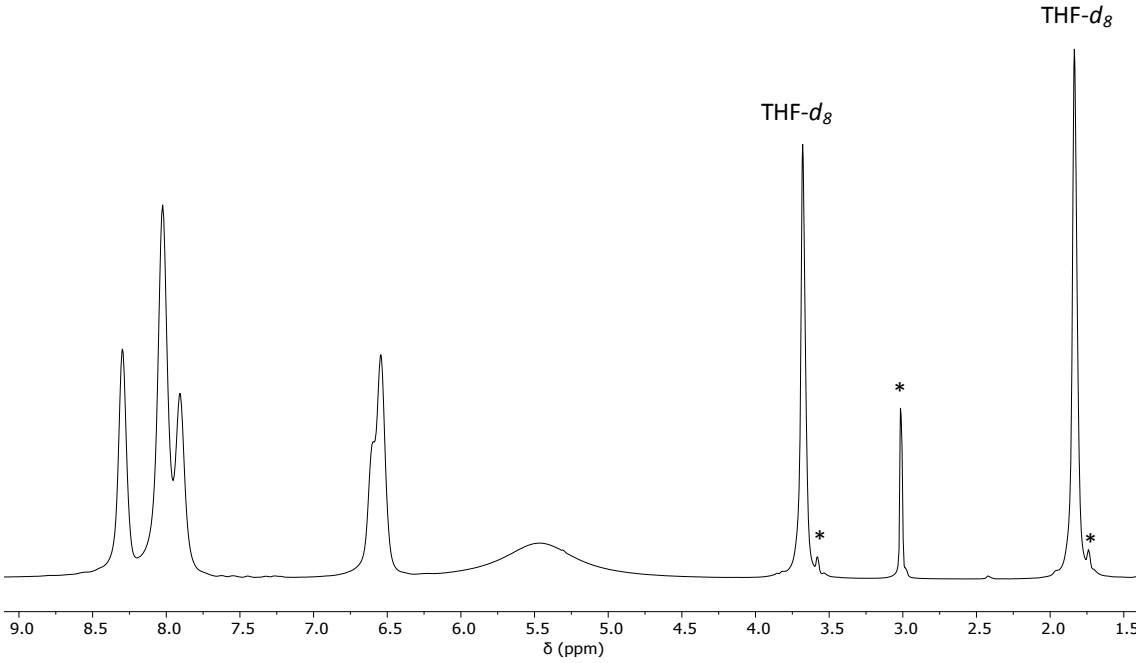

Figure S53. ^{1}H NMR spectrum of **6** (THF-d_8, 500 MHz, -65 °C).

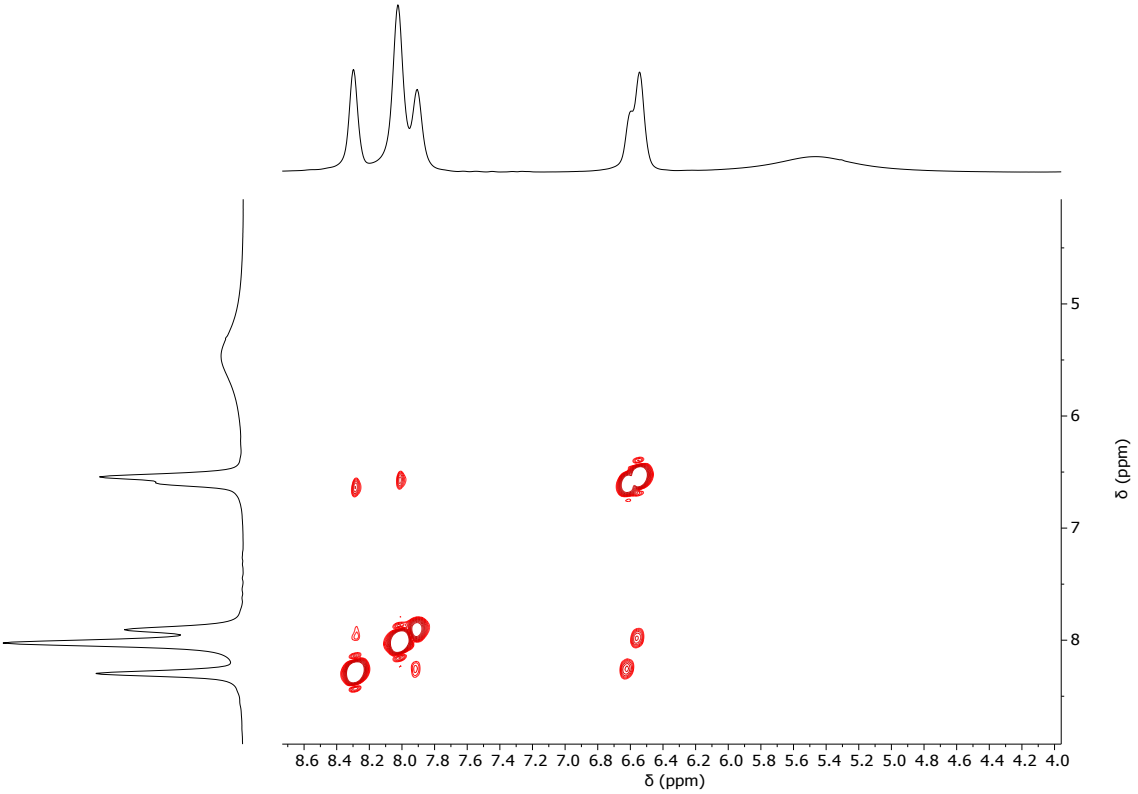

Figure S54. ^{1}H-^{1}H COSY spectrum of **6** (THF-d_8, 500 MHz, -65 °C).

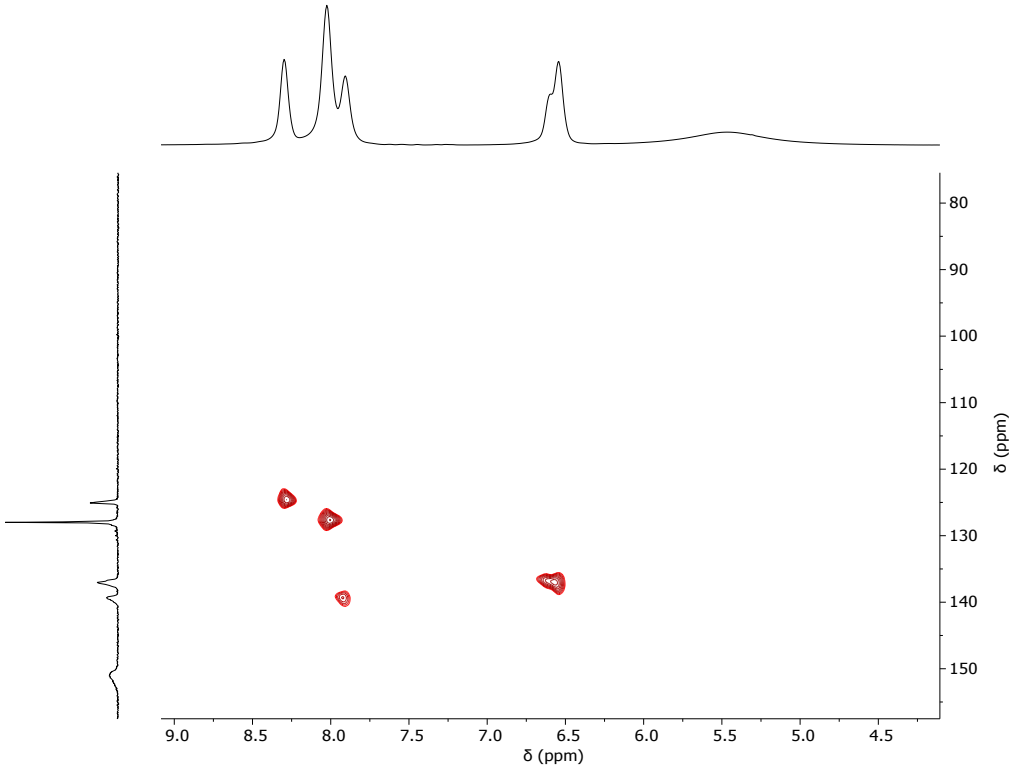

Figure S55. ^{1}H-^{13}C HMQC spectrum of **6** (THF-d_8, 500 MHz, -65 °C).

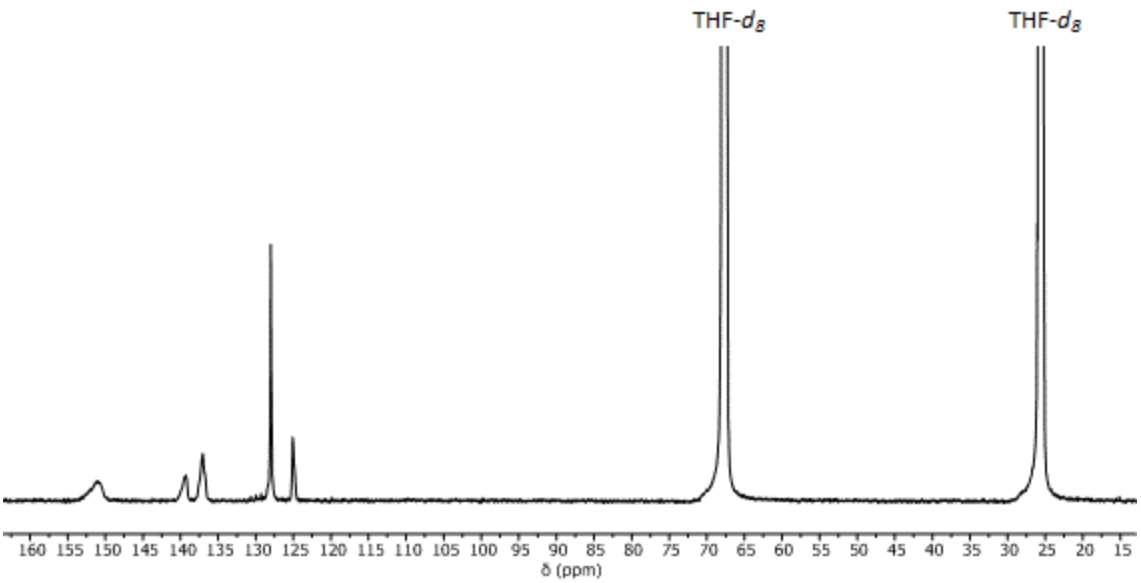

Figure S56. ^{13}C NMR spectrum of **6** (THF-d_8, 126 MHz, -65 °C).

Computational details

Density functional theory (DFT) calculations were performed using the Gaussian 09 code (revision D0.1),[19] using the OPBE exchange correlation functional.[20] A triple-ζ basis set with polarization functions on all atoms was employed.[21] All optimized structures are verified to be minima through the corresponding vibrational analysis. Computation of the Mössbauer parameters was done following the protocol developed by Neese, using the OPBE minima or X-ray crystallographic coordinates.[22]

Given the potential complexity of the electronic structure of iron formazanate complexes,[23] we subsequently performed CASSCF calculations at the OPBE minima using the ORCA 4.0 electronic structure suite.[24] Initially, an active space constructed with the 5 d-orbitals and 6 electrons was used, but this yielded a quintet ground state in disagreement with the experimental data. Expanding the active space with the π^*-orbitals from both ligands, i.e. CASSCF(6,7), reproduced the correct singlet ground state, which reveals the key role of the ligand π-type orbitals in obtaining a low-spin ground state in this class of compounds. Computation of thermochemical properties for comparison to experimental values using multi-reference methods is expensive, but the CASSCF data indicate that a single configuration is dominant (> 70%, see ESI) and we thus resorted to single-determinant DFT for thermochemistry.

All CASSCF calculations were performed with the ORCA computer code.[25] In these calculations, we employed the def2-TZVPP basis set,[26] including the corresponding auxiliary basis sets for correlation and Coulomb fitting. Two active spaces were used, the first containing 5 orbitals (the 5 d orbitals of the metal) and 6 electrons, and the second containing 7 orbitals (the 5 d orbitals of the metal and the 2 π-type metal-ligand orbitals) and 6 electrons. A spin−orbit coupling (SOC) correction has been included using the quasi-degenerate perturbation theory (QDPT) method as implemented in the current version of the ORCA code.[27] Intrinsic bond orbital analysis was performed using the IBOView program (version v20180510) develop by Knizia,[28] using the 'exponent 2' localization scheme.

Chart S1. Structure of compounds **1-7** used in the computational studies.

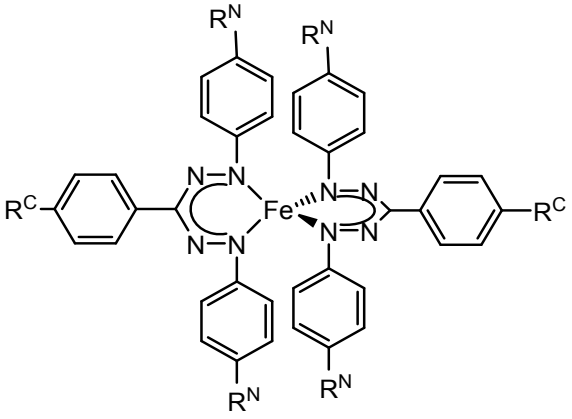

1 R^N = H; R^C = CH_3
2 R^N = F; R^C = CH_3
2' R^N = F; R^C = H
3 R^N = OCH_3; R^C = H
4 R^N = H; R^C = F
5 R^N = H; R^C = OCH_3
6 R^N = R^C = H
7 R^N = CH_3; R^C = CH_3

Table S9. Low-spin geometric parameters for systems **1**-**6** in the S=0 spin-state.

	1	**2**	**3**	**4**	**5**	**6**
Fe(1)–N(1)	1.823	1.823	1.824	1.823	1.823	1.823
Fe(1)–N(4)	1.823	1.823	1.824	1.823	1.823	1.823
Fe(1)–N(5)	1.823	1.823	1.824	1.823	1.823	1.823
Fe(1)–N(8)	1.823	1.823	1.824	1.823	1.823	1.823
N(1)–N(2)	1.307	1.308	1.309	1.307	1.307	1.308
N(3)–N(4)	1.307	1.308	1.309	1.307	1.307	1.308
N(5)–N(6)	1.307	1.308	1.309	1.307	1.307	1.308
N(7)–N(8)	1.307	1.308	1.309	1.307	1.307	1.308
∠(NFeN/NFeN) [a]	70.77	70.65	71.14	70.69	70.53	70.85

[a] angle between the coordination planes defined by the N-Fe-N atoms.

Table S10. High-spin geometric parameters for systems **1**-**6** in the S=2 spin-state.

	1	**2**	**3**	**4**	**5**	**6**
Fe(1)–N(1)	1.994	1.993	1.995	1.994	1.994	1.994
Fe(1)–N(4)	1.994	1.993	1.995	1.994	1.994	1.994
Fe(1)–N(5)	1.994	1.993	1.995	1.994	1.994	1.994
Fe(1)–N(8)	1.994	1.993	1.995	1.994	1.994	1.994
N(1)–N(2)	1.298	1.299	1.309	1.297	1.298	1.298
N(3)–N(4)	1.298	1.299	1.300	1.297	1.298	1.298
N(5)–N(6)	1.298	1.299	1.300	1.297	1.298	1.298
N(7)–N(8)	1.298	1.299	1.300	1.297	1.298	1.298
∠(NFeN/NFeN) [a]	83.60	83.85	84.60	83.49	83.55	83.60

[a] angle between the coordination planes defined by the N-Fe-N atoms.

Table S11. Molecular orbital energies (a.u.) for **1-7** in the low-spin (S = 0) state.

	1	**2'**	**3**	**4**	**5**	**6**	**7**
$\mathbf{d_{xy}}$	-0.0821	-0.0923	-0.0735	-0.0879	-0.0790	-0.0847	-0.0794
π*	-0.0964	-0.1063	-0.0865	-0.1023	-0.0940	-0.0987	-0.0932
π*	-0.1078	-0.1184	-0.0991	-0.1138	-0.1051	-0.1103	-0.1051
$\mathbf{d_{xz}}$	-0.1129	-0.1246	-0.1057	-0.1191	-0.1096	-0.1158	-0.1106
$\mathbf{d_{yz}}$	-0.1586	-0.1698	-0.1498	-0.1647	-0.1561	-0.1610	-0.1556
$\mathbf{d_{x2-y2}}$	-0.1766	-0.1875	-0.1675	-0.1827	-0.1738	-0.1792	-0.1737
$\mathbf{d_{z2}}$	-0.1900	-0.2010	-0.1811	-0.1962	-0.1871	-0.1926	-0.1872

Table S12. Normalized molecular orbital energies (a.u.) for **1-7** in the low-spin (S = 0) state, relative to the d_{yz} orbital set to E = 0 a.u.

	1	**2'**	**3**	**4**	**5**	**6**	**7**
$\mathbf{d_{xy}}$	0.0765	0.0775	0.0763	0.0768	0.0771	0.0763	0.0761
π*	0.0622	0.0635	0.0633	0.0624	0.0621	0.0623	0.0624
π*	0.0508	0.0515	0.0507	0.0509	0.0510	0.0507	0.0505
$\mathbf{d_{xz}}$	0.0456	0.0453	0.0441	0.0456	0.0465	0.0453	0.0449
$\mathbf{d_{yz}}$	0.0000	0.0000	0.0000	0.0000	0.0000	0.0000	0.0000
$\mathbf{d_{x2-y2}}$	-0.0181	-0.0177	-0.0177	-0.0180	-0.0177	-0.0182	-0.0181
$\mathbf{d_{z2}}$	-0.0314	-0.0312	-0.0313	-0.0315	-0.0310	-0.0316	-0.0316

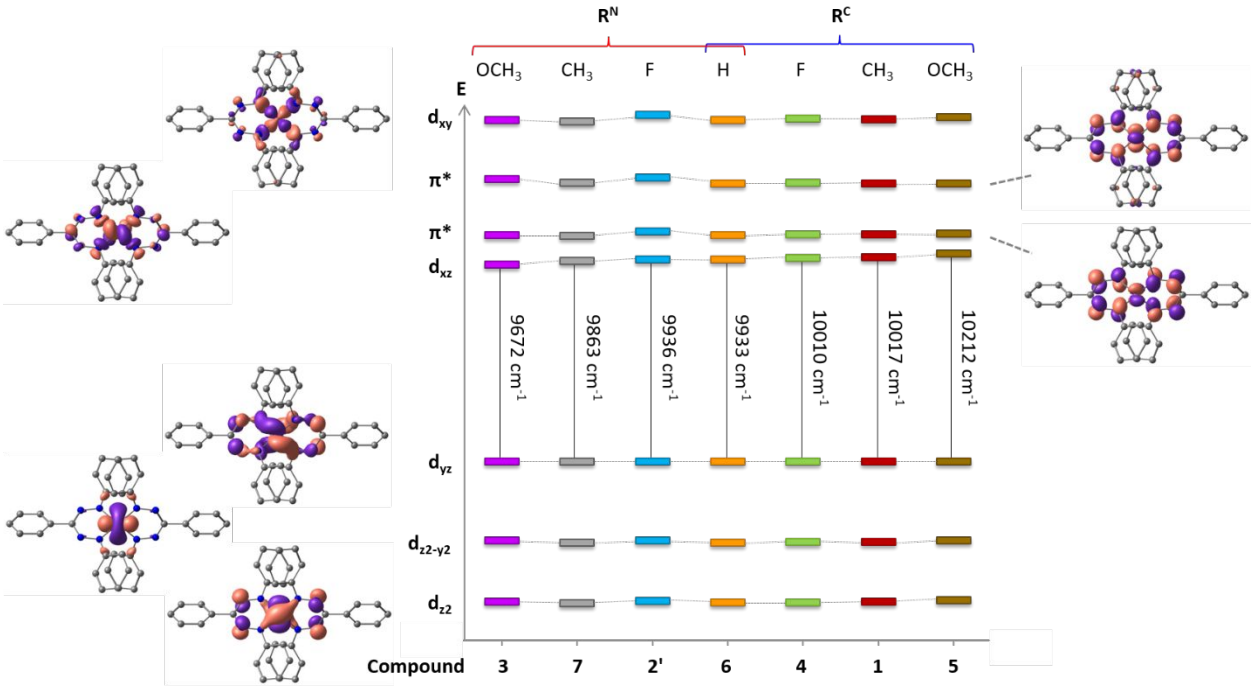

Figure S57. Molecular orbital diagram for **1-7** in the low-spin (S = 0) state.

Table S13. Experimental vs. computed ΔH and $T_{1/2}$. All energies are in KJ·mol^{-1} and all temperatures in K.

Compound	R^N	R^C	$\Delta H_{exp.}$	$\Delta H_{calc.}$	$T_{1/2(exp.)}$	$T_{1/2(calc.)}$
1	-H	-CH_3	18.8	9.50	346	154
2	-F	-CH_3	27.2	9.83	361	154
3	-OCH_3	-H	8.6	4.26	300	66
4	-H	-F	16.9	9.36	345	152
5	-H	-OCH_3	20.6	11.56	345	183
6	-H	-H	17.9	8.48	329	136

Table S14. Computed ΔH and $T_{1/2}$ for N-Ar *vs.* C-Ar functionalization of the bis(formazanate) iron(II) complexes. All energies are in $kJ \cdot mol^{-1}$ and all temperatures in K. The values for σ_P are the Hammett parameters.

Compound	R^N	R^C	σ_P (R^N)	σ_P (R^C)	Δ(HOMO-LUMO) (cm^{-1})	$\Delta H_{calc.}$
3	$-OCH_3$	-H	-0.268	0.000	9672	4.26
7	$-CH_3$	-H	-0.170	0.000	9863	6.75
6	-H	-H	0.000	0.000	9933	8.48
2'	-F	-H	+0.062	0.000	9936	8.68
5	-H	$-OCH_3$	0.000	-0.268	10212	11.56
1	-H	$-CH_3$	0.000	-0.170	10017	9.50
6	-H	-H	0.000	0.000	9933	8.48
4	-H	-F	0.000	+0.062	10010	9.46

Table S15. Contribution from the main determinants to the ground state of the multiconfigurational wavefunction.

Compound	R^N	R^C	Root0	Root1	Root2
1	-H	$-CH_3$	0.72128	0.27281	0.00376
2	-F	$-CH_3$	0.74506	0.24887	0.00353
3	$-OCH_3$	-H	0.72108	0.17250	0.10543
4	-H	-F	0.70521	0.28870	0.00397
5	-H	$-OCH_3$	0.73179	0.20115	0.06077
6	-H	-H	0.70620	0.28822	0.00335

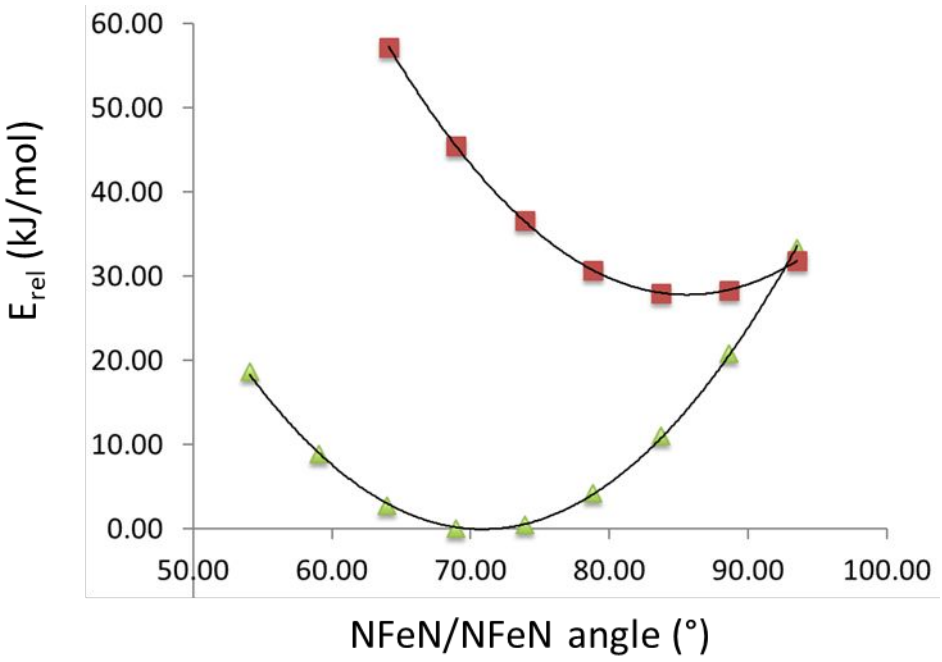

Figure S58. Electronic energy of the low-spin (green triangles) and high-spin (red squares) state of compound **6** as a function of NFeN/NFeN dihedral angle. Values are relative to the minimum on the low-spin surface.

References

(1) Gilroy, J. B.; Ferguson, M. J.; McDonald, R.; Patrick, B. O.; Hicks, R. G. Formazans as β-diketiminate analogues. Structural characterization of boratatetrazines and their reduction to borataverdazyl radical anions *Chem. Commun.* **2007**, 126.
(2) Broere, D. L.; Coric, I.; Brosnahan, A.; Holland, P. L. Quantitation of the THF Content in Fe[N(SiMe3)2]2.xTHF *Inorg Chem* **2017**, *56*, 3140.
(3) Turbiak, A. J.; Showalter, H. D. A novel synthesis of N(1)-(substituted)-pyrimido[5,4-e]-1,2,4-triazine-5,7(1H,6H)-diones *Tetrahedron Lett* **2009**, *50*, 1996.
(4) Maar, R. R.; Barbon, S. M.; Sharma, N.; Groom, H.; Luyt, L. G.; Gilroy, J. B. Evaluation of Anisole-Substituted Boron Difluoride Formazanate Complexes for Fluorescence Cell Imaging *Chemistry* **2015**, *21*, 15589.
(5) Katritzky, A. A.; Belyakov, S. A.; Cheng, D.; Durst, H. D. Syntheses of Formazans Under Phase-Transfer Conditions *Synthesis* **1995**, *1995*, 577.
(6) (a) Tezcan, H.; Can, Ş.; Tezcan, R. The synthesis and spectral properties determination of 3-substituted phenyl-1,5-diphenylformazans *Dyes and Pigments* **2002**, *52*, 121. (b) Shuki, A.; Naomitsu, A.; Yasuo, B. Syntheses and Properties of Quinonoid Mesoionic Compounds *Bulletin of the Chemical Society of Japan* **1989**, *62*, 1612.
(7) Travieso-Puente, R.; Broekman, J. O. P.; Chang, M.-C.; Demeshko, S.; Meyer, F.; Otten, E. Spin-Crossover in a Pseudo-tetrahedral Bis(formazanate) Iron Complex *J. Am. Chem. Soc.* **2016**, *138*, 5503.
(8) Momma, K. I., F. VESTA 3 for three-dimensional visualization of crystal, volumetric and morphology data *Journal of Applied Crystallography* **2011**, *44*, 1272.
(9) Wolfram Research, I., *Mathematica*, **2019**, Wolfram Research, Inc.
(10) (a) Kläui, W. E., W.; Gütlich, P. Spin-Crossover Cobalt(III) Complexes: Steric and Electronic Control of Spin State *Inorganic Chemistry* **1987**, *26*, 3977. (b) Lin, H. J.; Siretanu, D.; Dickie, D. A.; Subedi, D.; Scepaniak, J. J.; Mitcov, D.; Clerac, R.; Smith, J. M. Steric and electronic control of the spin state in three-fold symmetric, four-coordinate iron(II) complexes *J Am Chem Soc* **2014**, *136*, 13326. (c) Gütlich, P., Goodwin, Harold A. *Spin Crossover in Transition Metal Compounds I*; 1st ed.; Springer-Verlag Berlin Heidelberg, 2004.
(11) Van Geet, A. L. Calibration of the methanol and glycol nuclear magnetic resonance thermometers with a static thermistor probe *Analytical Chemistry* **1968**, *40*, 2227.
(12) Atkins, P. d. P., J. *Physical Chemistry*; 8th ed.; Oxford University Press: Oxford, United Kingdom,, 2006; Vol. Chapter 5.
(13) Chang, M.-C.; Dann, T.; Day, D. P.; Lutz, M.; Wildgoose, G. G.; Otten, E. The Formazanate Ligand as an Electron Reservoir: Bis(Formazanate) Zinc Complexes Isolated in Three Redox States *Angew. Chem. Int. Ed.* **2014**, *53*, 4118.
(14) Evans, D. F. The determination of the paramagnetic susceptibility of substances in solution by nuclear magnetic resonance *Journal of the Chemical Society* **1959**, 2003.
(15) Ostfeld, D.; Cohen, I. A. A cautionary note on the use of the Evans method for magnetic moments *Journal of Chemical Education* **1972**, *49*, 829.
(16) Grant, D. H. Paramagnetic Susceptibility by NMR: The "Solvent Correction" Reexamined *Journal of Chemical Education* **1995**, *72*, 39.
(17) Schubert, E. M. Utilizing the Evans method with a superconducting NMR spectrometer in the undergraduate laboratory *Journal of Chemical Education* **1992**, *69*, 62.
(18) Bain, G. A.; Berry, J. F. Diamagnetic Corrections and Pascal's Constants *J. Chem. Educ.* **2008**, *85*, 532.
(19) Frisch, M. J.; Trucks, G. W.; Schlegel, H. B.; Scuseria, G. E.; Robb, M. A.; Cheeseman, J. R.; Scalmani, G.; Barone, V.; Mennucci, B.; Petersson, G. A.; Nakatsuji, H.; Caricato, M.; Li, X. H., H. P.; Izmaylov, A. F.; Bloino, J.; Zheng, G.; Sonnenberg, J. L.; Hada, M.; Ehara, M.; Toyota, K.; Fukuda, R.; Hasegawa, J.; Ishida, M.; Nakajima, T.; Honda, Y.; Kitao, O.; Nakai, H.; Vreven, T.; Montgomery Jr., J. A.; Peralta, J. E.; Ogliaro, F.; Bearpark, M. J.; Heyd, J.; Brothers, E. N.; Kudin, K. N.; Staroverov, V. N.; Kobayashi, R.; Normand, J.; Raghavachari, K.; Rendell, A. P.; Burant, J. C.; Iyengar, S. S.; Tomasi, J.; Cossi, M.; Rega, N.; Millam, N. J.; Klene, M.; Knox, J. E.; Cross, J. B.; Bakken, V.; Adamo, C.; Jaramillo, J.; Gomperts, R.; Stratmann, R. E.; Yazyev, O.; Austin, A. J.; Cammi, R.; Pomelli, C.; Ochterski, J. W.; Martin, R. L.; Morokuma, K.; Zakrzewski, V. G.; Voth, G. A.; Salvador, P.; Dannenberg, J. J.; Dapprich, S.; Daniels, A. D.; Farkas, Ö.; Foresman, J. B.; Ortiz, J. V.; Cioslowski, J.; Fox, D. J., *Gaussian 09, Rev. D01*, **2009**,

(20) (a) Hoe, W. M.; Cohen, A. J.; Handy, N. C. Assessment of a new local exchange functional OPTX *Chem. Phys. Lett.* **2001**, *341*, 319. (b) Handy, N. C.; Cohen, A. J. Left-right correlation energy *Mol. Phys.* **2001**, *99*, 403. (c) Perdew, J. P.; Burke, K.; Ernzerhof, M. Generalized gradient approximation made simple *Phys. Rev. Lett.* **1996**, *77*, 3865. (d) Perdew, J. P.; Burke, K.; Ernzerhof, M. Generalized Gradient Approximation Made Simple [Phys. Rev. Lett. 77, 3865 (1996)] *Phys. Rev. Lett.* **1997**, *78*, 1396.
(21) Schafer, A.; Huber, C.; Ahlrichs, R. Fully Optimized Contracted Gaussian-Basis Sets of Triple Zeta Valence Quality for Atoms Li to Kr *J. Chem. Phys.* **1994**, *100*, 5829.
(22) Römelt, M.; Ye, S.; Neese, F. Calibration of Modern Density Functional Theory Methods for the Prediction of 57Fe Mössbauer Isomer Shifts: Meta-GGA and Double-Hybrid Functionals *Inorganic Chemistry* **2009**, *48*, 784.
(23) Broere, D. L. J.; Mercado, B. Q.; Lukens, J. T.; Vilbert, A. C.; Banerjee, G.; Lant, H. M. C.; Lee, S. H.; Bill, E.; Sproules, S.; Lancaster, K. M.; Holland, P. L. Reversible Ligand-Centered Reduction in Low-Coordinate Iron Formazanate Complexes *Chem. Eur. J.* **2018**, *24*, 9417.
(24) (a) Neese, F. The ORCA program system *Wiley Interdiscip. Rev. Comput. Mol. Sci.* **2012**, *2*, 73. (b) Neese, F. Software update: the ORCA program system, version 4.0 *Wiley Interdiscip. Rev. Comput. Mol. Sci.* **2018**, *8*, e1327.
(25) Neese, F. Software update: the ORCA program system, version 4.0 *WIREs Computational Molecular Science* **2018**, *8*.
(26) Weigend, F.; Ahlrichs, R. Balanced basis sets of split valence, triple zeta valence and quadruple zeta valence quality for H to Rn: Design and assessment of accuracy *Phys Chem Chem Phys* **2005**, *7*, 3297.
(27) Hose, G.; Kaldor, U. Quasidegenerate perturbation theory *The Journal of Physical Chemistry* **1982**, *86*, 2133.
(28) Knizia, G. Intrinsic Atomic Orbitals: An Unbiased Bridge between Quantum Theory and Chemical Concepts *Journal of Chemical Theory and Computation* **2013**, *9*, 4834.